Università degli Studi di Ferrara

DOTTORATO DI RICERCA IN
Fisica

CICLO XXI

COORDINATORE Prof. Filippo Frontera

Surface interaction mechanisms in metal-oxide semiconductors for alkane detection

Settore Scientifico Disciplinare FIS/01

Dottorando
Dott. Delia Puzzovio

Tutore
Prof. Vincenzo Guidi

Anni 2006/2008

Contents

CONTENTS

Introduction

Solid state gas sensors represent a remarkable application of modern nanotechnologies and complex physico-chemical processes. These devices transduce a chemical quantity, such as a gas concentration, into an electric signal.

Gas sensors based on semiconductive materials have gained an increasing interest, thanks to their advantageous characteristics in comparison with traditional systems (based on optics and spectroscopic analysis), which are more cumbersome, expensive and require a careful maintenance by qualified personnel. On the other hand, solid state devices are characterised by small encumbrance, easy usage, low-cost, reliability, high sensitivity and repeatability. However, sensor electric properties are also influenced by the interaction with molecules of gases present in the atmosphere other than the target gas. It is difficult to eliminate the effect of interfering gases, whose signal may overcome that of the gas of interest. This intrinsic lack of selectivity made research in this field to come to a standstill and hindered a significant development of such sensors. Additivation of sensitive material by means of catalysts (such as Pd, Pt and Au) seems to be a viable way to promote or hinder a chemical reaction instead of another. Nonetheless, experiments have not solved this problem yet. Another solution is the usage of filtres, though the number of experimental studies in this direction is meagre.

Semiconductor gas sensors are mainly applied to environmental monitoring, in order to keep pollutant gas concentrations under control, because of their negative effects on human health and on monuments. Also indoor applications are very useful, e.g. for the detection of gas leaks from both heating system and gas kitchen. For these reasons, researchers have concentrated their studies towards gases like CO, CO_2, NO_x and alkanes.

Light alkanes have been widely studied for many years especially in catalysis. Their behaviour is relatively easy to understand because of their simple molecules. Therefore,

a great number of publications appears in literature with theories and results concerning alkane reaction mechanisms. Moreover, these gases are very interesting also for gas sensing. Methane and propane have been extensively used for combustion, propane is employed for the production of hydrogen by steam-reforming plants, and i-butane is recognised to be very useful in charge particle detection in nuclear physics.

A clearer analysis of surface reaction phenomena is the key to find a solution to the problem of limited selectivity. This approach has been applied to gases of great interest, such as alkanes. The main aim of this dissertation is to clarify some theoretical and experimental aspects related to the sensing processes of metal-oxide semiconductors, studying their surface and conduction properties.

The first chapter deal with the electronic behaviour and the conduction mechanism of metal oxides, whereas the second contains a general view of gas adsorption processes. The synthesis and the deposition methods, employed for the production of the sensitive powders and of the thick film sensors, are described in chapter 3. The subsequent chapters are dedicated to the experimental measurements. First, surface interactions between metal-oxide powders and oxygen were analysed by means of temperature-programmed desorption techniques. The results of desorption experiments, performed at the *IRCELYON* (*Institut de Recherches sur la Catalyse et l'Environnement de Lyon*), are presented and discussed in chapter 4. In the end, sensing of light alkanes was studied. Chapter 5 comprises an explanation of the reaction mechanisms between alkanes and the surface of the sensors and the discussion of the results of conduction measurements, carried out at the *Sensor and Semiconductor Laboratory* of Ferrara.

Chapter 1

Metal-oxide semiconductors: electronic behaviour and working mechanism

Metal-oxide semiconductors are widely studied and used as raw materials for chemoresistive gas sensors. These devices are found to be very useful in the detection of toxic and pollutant gases. Indeed, they are recognised to have established advantages such as low cost, compactness and ease of integration with integrated circuit technology.

As Wagner and Hauffe [1] discovered in 1938, adsorbed atoms and molecules on the surface of a semiconductor influence its properties, such as conductivity and surface potential. Later, many researchers [2, 3, 4] studied these effects on semiconductor electric conductance. The first applications of these discoveries arrived soon after [5, 6] together with the production of the first chemoresistive-semiconductor-gas sensors. Since that moment, technology development and the problem of toxic and pollutant gas monitoring encouraged improvements in the production and in the performances of different kind of gas sensors.

A large part of commercial gas sensors are built with SnO_2, while TiO_2 and ZrO_2 are often employed for devices aimed towards combustion monitoring.

1.1 Bulk and band model

Electrons in a crystal can only adopt energy values which stay inside certain ranges or more specifically *bands* of energy. Energy bands are separated from prohibited energy bands, called *band gap* [7]. In a semiconductor the highest energy band occupied by fundamental state electrons is called *valence band*, while the upper band, in which electrons can be promoted, is called *conduction band*. Conduction band would be completely empty in a perfect crystal at 0 K. However, we remark that solids have an imperfect structure, as a consequence electrons are present in the conduction band or miss in the valence one. Therefore, semiconductors applied on gas sensing are based on the fact that electrons could be transferred or removed from the conduction band, in order to induce consistent variations in the conductivity of the material.

Semiconductor band model is depicted in Fig. 1.1, where electron energy is on the x-axis, while the distance inside the crystal is on the y-axis. The energy gap E_g represents the demanded energy for valence electron excitation (promotion to conduction band). Electron distribution in the different energy levels under thermal equilibrium condition is given by the function of *Fermi* f:

$$f = \frac{1}{1 + e^{\frac{E - E_F}{kT}}} \tag{1.1}$$

Where k is the Boltzmann constant and T is the absolute value of temperature. This function expresses the probability that an energy level E is occupied by an electron. The *energy of Fermi* is that value of energy E_F where f=1/2, that is to say that an energy level equal to E_F has the same probability of being full or empty.

SnO_2 is a semiconductor with an energy gap of 3.6 eV. n-type conductivity is due to the oxygen vacancies derived from the typical stoichiometric defects of the material. These vacancies can be singly or doubly ionized and they act as donor states with energy levels positioned at 0.03 and 0.015 eV under the bottom of the conduction band. Therefore, they give electrons to the conduction band and enhance the conductance of the material. As a consequence of this overpopulation of electrons in the conduction band, the Fermi level is raised. Assuming $E_C - E_F > 2kT$, where E_C is the lower limit of the conduction band,

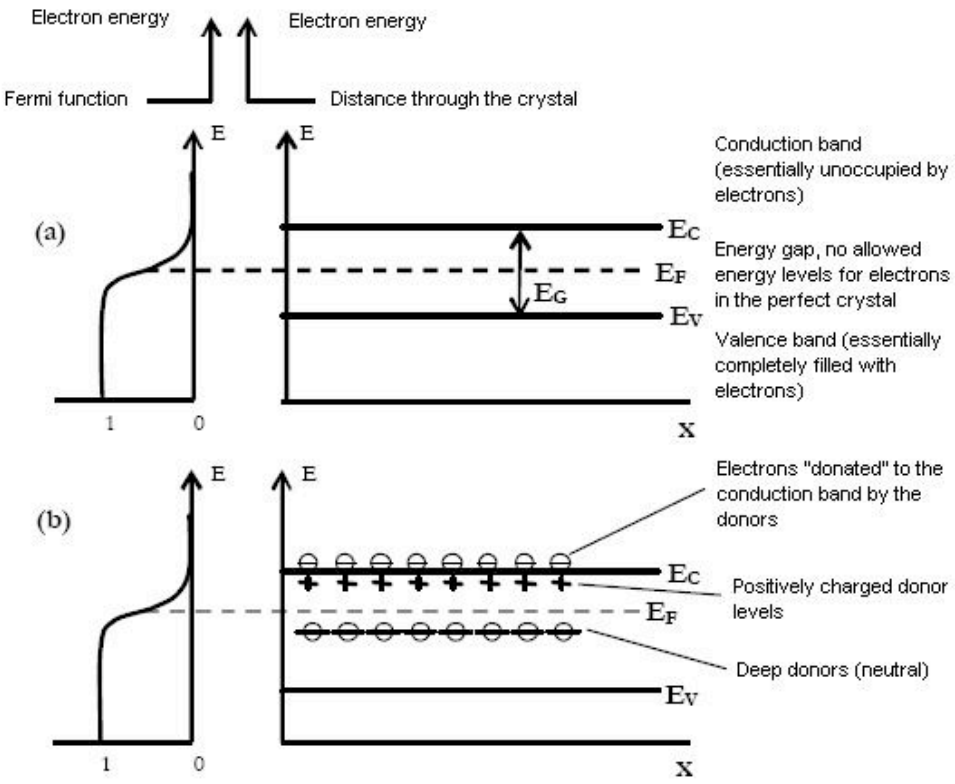

Figure 1.1: *Fermi function and band diagram for semiconductors; (a) intrinsic semiconductor; (b) n-type semiconductor with deep and shallow donors.*

the electron density, n, can be written (employing Boltzmann approximation, for which f is reduced to a simple exponential, if E-E$_F$ $\gg$ kT) [7]:

$$n = N_C \cdot e^{-(E_C - E_F)/kT} \tag{1.2}$$

where N$_C$ is the effective density of the states next to the bottom of the conduction band.

1.2 Intrinsic surface states

A sudden interruption of the crystal lattice periodicity occurs on the surface. Thus, surface atoms or ions have an incomplete coordination number (number of first neighbours), which causes a rearrangement and a greater reactivity in comparison to that of bulk atoms or ions. The perturbation of lattice periodicity is enough to create *intrinsic* localised electronic states at surface level [9].

In ionic materials, as many metal oxide semiconductors are, every surface ion, having incomplete coordination, is even not coupled with the opposite charge ion. In a metal oxide, metal cations tend to catch electrons behaving as *acceptors*, while oxygen anions tend to release electrons behaving as *donors*. In this last case, one can visualise the electron as not coupled in an orbital, which extends up till outside the surface. Now, it is ostensible that this electron could both accept another electron to create a couple and enter in the bulk, leaving a unoccupied surface state.

In the end, it is possible to say that both energy levels, acceptors and donors, are present on the surface of the crystal. Fig. 1.2 shows a band model which includes the surface of the crystal and indicates the presence of surface states [7]. The case when there is no net charge is used for simplicity. This is the so-called *flat-band case*. As one can observe, all surface states are not at the same energy.

1.2.1 Double layer

Considering again Fig. 1.2 for n-type semiconductor, it must be underlined that the flat-band case cannot be an equilibrium situation. The electrons in the conduction band are at a much higher energy level than the energy level of the acceptor surface states. Thus,

1.2 Intrinsic surface states

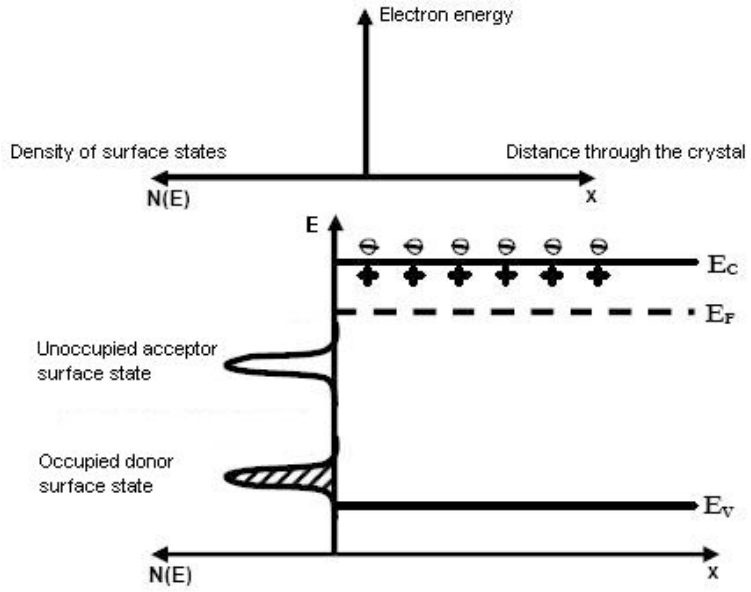

Figure 1.2: *Surface states bands at the n-semiconductor surface. In the diagram, the surface states are assumed to be neutral (acceptor states are unoccupied and donor states are occupied). For simplicity in many arguments, the bands of surface states can be represented as single energy levels.*

they will move from the conduction band to those lower-energy states, forced by this new energetically more favourable configuration. With the upper levels (acceptors) completely empty and the lower levels (donors) completely full, by definition the Fermi energy must be in between. Therefore, the electrochemical potential of the electrons at the surface states is lower than that in the conduction band. Thereby, electrons will have to move towards the surface states. When such transitions occur, a charge builds up at the surface and a *countercharge* in the bulk (the *countercharge* being that of the donor ions).

Fig. 1.3 shows an n-type semiconductor after the charge has moved from the donor ions to the surface states. A *double layer* is formed, with the positively charged donors in the semiconductor as *space-charge layer* on the one side, and the negatively charged surface states as a sheet of charges on the other side. Thus, an electric field develops between these two charge layers. The term *space-charge layer* refers to the region, where the uncompensated donor ions are the only important charged species. The charge density from such ions is N_i=N_D-N_A, where N_D is the donor density and N_A is the acceptor density. The term *depletion layer* is used to describe this region, because all the mobile carriers (in figure 1.3, the electrons) have been exhausted from the region and moved to the surface [7].

A scheme of two grains of metal-oxide powder is depicted in Fig. 1.4, where the space-charge region around the surface and at the contact point is shown. The oxygen species adsorbed create the surface-charge layer, which is responsible for the intergranular potential barrier that conduction electrons have to overcome, in order to go from a grain to another.

1.2.2 The equation of Poisson

The one-dimensional equation of Poisson states:

$$\frac{d^2\Phi}{dx^2} = \frac{qN_i}{\epsilon}\epsilon_0 \tag{1.3}$$

where ϕ is the potential, N_i is the net density of ions in the space-charge region, ϵ is the dielectric constant of the semiconductor, and ϵ_0 is the permittivity of free space. The donor density N_D (for n-type material) or acceptor density N_A (for p-type material) is indepen-

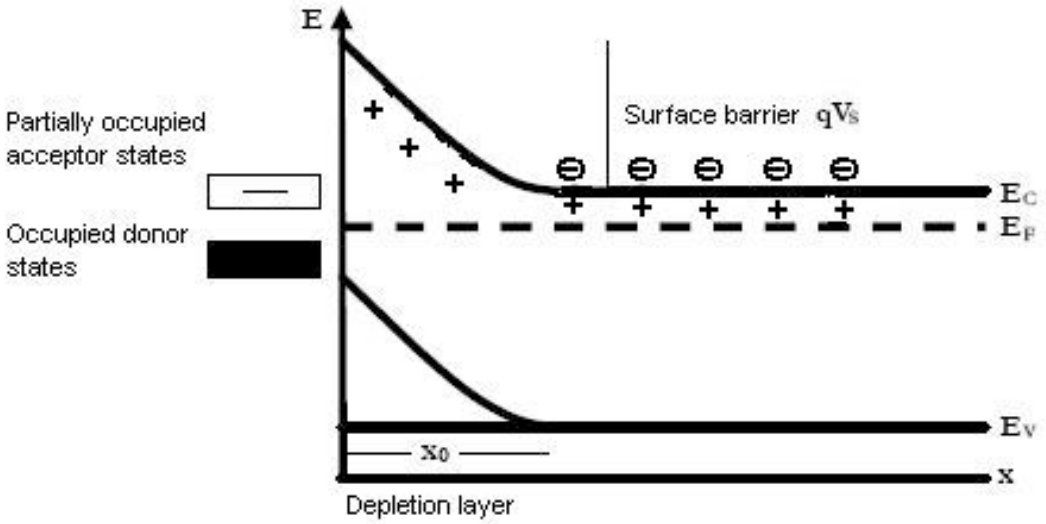

Figure 1.3: *Double layer. Electrons from the conduction band are captured by surface states, leading to a negatively charged surface with the counter-charge the positively charged donors near the surface.*

dent of x (the distance into the crystal), in general, because the donors or acceptors have been introduced into the material in such a way as to make them independent of distance (homogeneous doping). A change in coordinates is helpful in relating the mathematics to the band diagram, where, rather than potential, the energy of an electron is plotted. We define to that end the parameter V as:

$$V(x) = \Phi_b - \Phi(x) \tag{1.4}$$

where Φ_b is the potential in the bulk of the semiconductor. Then the first integration of Poisson's equation is straightforward:

$$\frac{dV}{dx} = \frac{qN_i(x - x_0)}{\epsilon\epsilon_0} \tag{1.5}$$

where x_0 is the thickness of the space-charge region. The thickness of the space-charge region is determined by the distance necessary to compensate all the surface charge. At

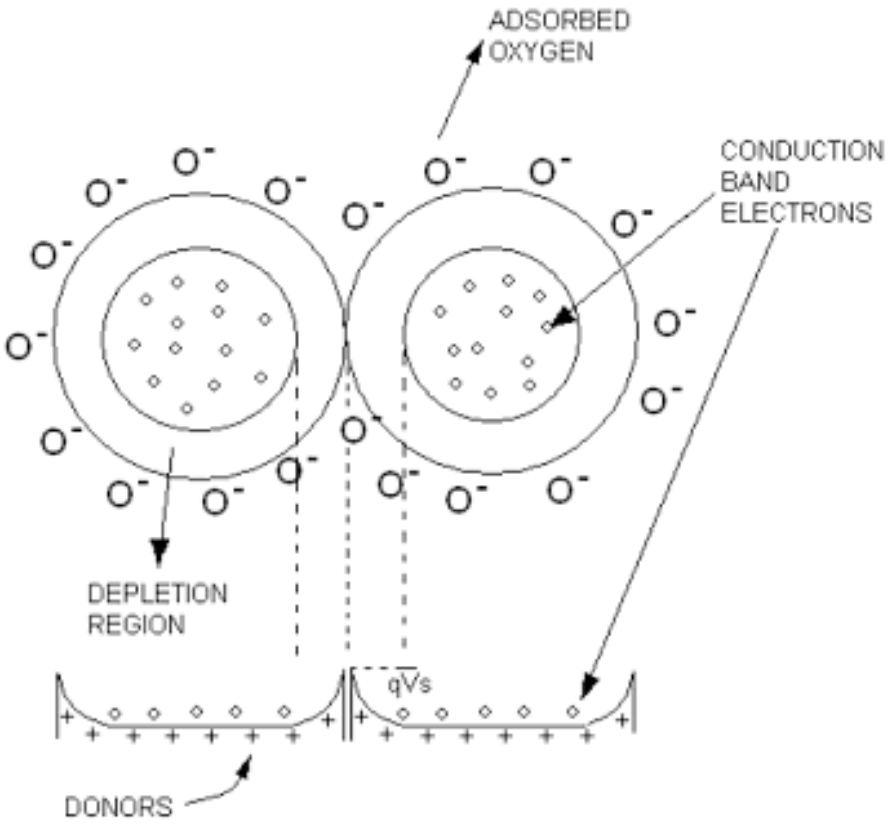

Figure 1.4: *Potential barrier between grains.*

$x \geq x_0$ the semiconductor is uncharged, so we use the boundary condition that dV/dx=0 at x=x_0. For n-type material $N_D x_0 (= N_i x_0)$ is the number of electrons (per unit area) extracted from the surface region of thickness x_0, and this equals the number of electrons (per unit area) moved to the surface:

$$N_i x_0 = N_s \tag{1.6}$$

where N_s is the density of charged surface states. The integration of 1.5 leads to:

$$V = \frac{qN_i(x - x_0)^2}{2\epsilon\epsilon_0} \tag{1.7}$$

because V was defined zero at x=x_0. This leads to the relation of Schottky; the value of the surface barrier V_s (V at x=0) is

$$V_s = \frac{qN_i x_0^2}{2\epsilon\epsilon_0} \tag{1.8}$$

The energy qV_s is the energy that electrons must attain before they can move to surface energy levels. In the end, using 1.6 to eliminate x_0 from 1.8, the following expression is obtained:

$$V_s = \frac{qN_s^2}{2\epsilon\epsilon_0 N_i} \tag{1.9}$$

an important relation describing the potential difference between the surface and the bulk (or, as qV_s, the energy difference of electrons between the surface and the bulk) as a function of the amount of charge N_s on the surface. In the above calculus, the charge was assumed to be on clean surface, but equally well the charge can be associated, for example, to the density of negatively charged adsorbed oxygen (e.g., O_2^-), of critical interest for semiconductor gas sensors operating in air.

1.2.3 Spherical model and limits to the depletion approximation

The barrier of Schottky is usually studied within the depletion approximation in plane geometry. However, when considering a grain with radius R comparable to the dimension of the depletion region, the curvature effects become relevant and some modifications are necessary [10].

First of all, the equation of Poisson is solved in spherical symmetry:

$$\frac{1}{r}\frac{d^2}{dr^2}[r\Phi(r)] = -\frac{qN_d}{\epsilon} \tag{1.10}$$

where N_d is the density of donors, which are supposed to be completely ionised at the working temperature. R is defined as the radius of the grain, while R_0 the radius of the neutral region (see Fig. 1.5). When considering the depletion approximation, the density of charge is qN_d in the whole region thick R-R_0 (x_0 in par. 1.2.2) and zero elsewhere. Moreover, another hypothesis is that Φ_r becomes zero for r=R_0, that is to say that the electric field -$\nabla\Phi$(r) is zero for r$\leq R_0$. It has to be remarked that in this approximation R-R_0 represents both the thickness of the depletion region and the length of the potential extinction.

The difference between the potential in the centre of the grain and that on the surface is called the *built-in potential V*. Therefore, the following initial conditions are imposed to Eq. 1.10:

$$[\Phi(r)]_{R_0} = 0 \qquad -\nabla\Phi(r)|_{R_0} = 0 \tag{1.11}$$

and they lead to an analytical solution for the electric potential:

$$\Phi(r) = -\frac{qN_d}{6\epsilon}r^2 - \frac{qN_d}{3\epsilon}\frac{R_0^3}{r} + \frac{qN_d}{2\epsilon}R_0^2 \tag{1.12}$$

at $R_0 \leq$r$\leq$R and zero elsewhere. Now, there is a Coulombian-like term, emerging from the spherical symmetry and becoming relevant when $R_0 \to 0$. This term does not appear in the planar symmetry, where there is just a parabolic dependence.

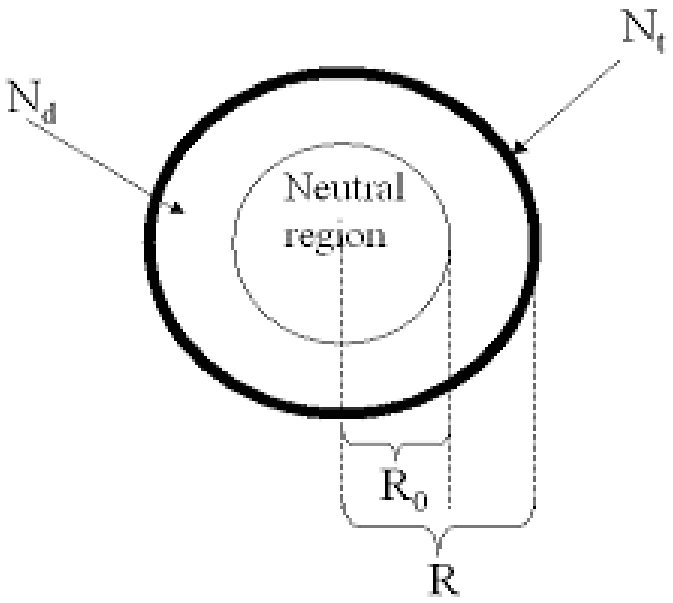

Figure 1.5: *Scheme of a grain, where N_t is the surface density of acceptors and N_d is the density of donors in the depletion region.*

It is worth remarking that the grain must be altogether neutral, so that the surface charge density, qN_t, exactly compensates for the space charge in the depleted region. This implies:

$$N_t = N_d \left(\frac{R}{3} - \frac{R_0^3}{3R^2} \right) \tag{1.13}$$

The spherical model just described is still based on the depletion approximation, which unfortunately fails, when the dimension of the grain goes down a limit value.
When considering an n-type semiconductor, the charge density must be expressed as follows:

$$\rho(r) = qN_d - qN_d e^{q\Phi(r)/kT} \tag{1.14}$$

where the second term is the contribution of the mobile charge carrier at nonzero temperature.

The charge density used in the depletion approximation must be achievable from Eq. 1.14, in which the zero of energy (and potential) is fixed at E_{CBB} (bulk) (CBB means conduction band bottom). However, in the case of powdered or polycrystalline semiconductors, the bulk can be reached only if the grain is sufficiently large, while the depletion approximation assumes that the zero-potential is always attained, independently of the grain size. Thus, when it is not possible to apply the approximation, we have to solve the following equation in spherical coordinates:

$$\frac{1}{r}\frac{d^2}{dr^2}[r\Phi(r)] = -\frac{qN_d}{\epsilon} + \frac{qN_d}{\epsilon} e^{q\Phi(r)/kT} \tag{1.15}$$

In this case, the boundary conditions are different from those used in the depletion approximation. The spherical symmetry makes the field equal zero in the centre of the grain, while the potential is set at zero at the CBB in the centre of a sufficiently large grain. Moreover, the charge density (Eq. 1.14) should be modified. When referred to this zero, the surface potential $\Phi(R)$ assumes a value that is univocally determined by the working conditions (semiconductor, doping, temperature and environment) and is independent of

R. Defining this values as -V_s, we set the second boundary condition for Eq. 1.15:

$$\Phi(R) = -V_s \tag{1.16}$$

However, a difficulty arises, when we want to compare V_s with what can be experimentally measured. The methods employed commonly to determine the surface potential measure the built-in potential V=Φ(0)-Φ(R) (the difference between the potential at the CBB in the centre, $\Phi(0)$, and the potential at the surface, Φ(R)). If R$\geq \Xi$ (where Ξ is the potential extinction length), ϕ can be considered zero and the measured value V coincides with V_s. In the case of a small grain, the boundary condition Φ(R)=-V is not correct.

As for the depletion approximation, the neutrality of the grain is imposed. This means that the integral of the charge density in Eq. 1.14 over the entire volume of the grain equals the integration of the surface acceptor state density N_t, which is assumed to be uniform over the surface:

$$4\pi \int_0^R \left(qN_d - qN_d e^{q\Phi(r)/kT}\right) r^2 dr = 4\pi R^2 q N_t \tag{1.17}$$

Therefore, the system of equations constituting the model based on the complete charge density is:

$$\begin{aligned} \tfrac{1}{r}\tfrac{d^2}{dr^2}[r\Phi(r)] &= -\tfrac{qN_d}{\epsilon} + \tfrac{qN_d}{\epsilon} e^{q\Phi(r)/kT}, \\ -\tfrac{d\Phi(r)}{dr}|_{r=0} &= 0, \\ \Phi(r)|_{r=R} &= -V_b, \\ -\tfrac{d\Phi(r)}{dr}|_{r=R^-} &= \tfrac{qN_t}{\epsilon} \end{aligned} \tag{1.18}$$

The last equation is derived from the neutrality condition of Eq. 1.17. The model is based on six parameters (T, ϵ, V_b, N_d, N_t and R) and one unknown function (Φ(r)). N_d and ϵ characterise the semiconductor and can be directly measured with T. The value of V_s for a specific semiconductor at a certain temperature depends only on the environment and

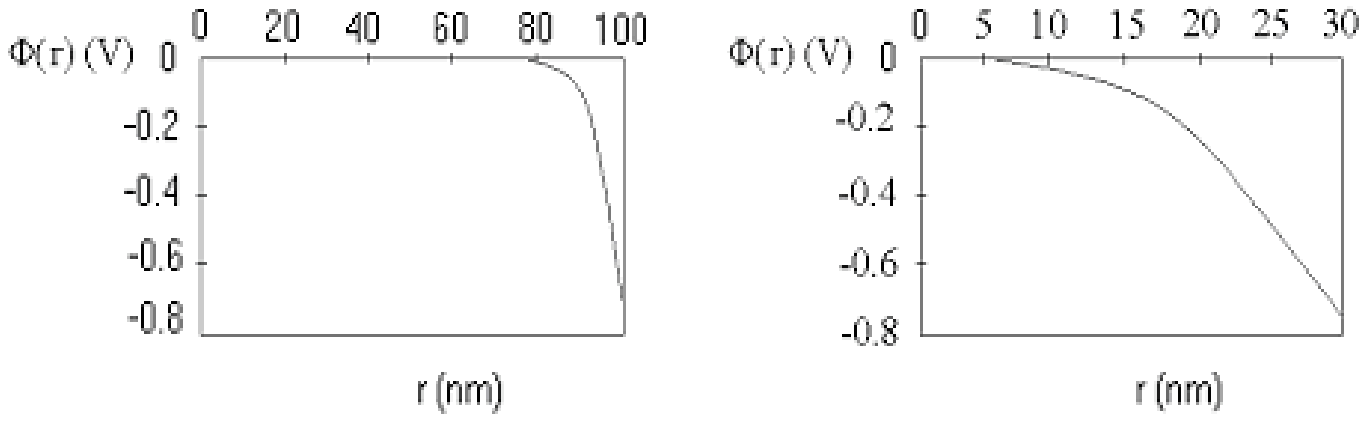

Figure 1.6: *Potential shape vs coordinate r for R=100 nm (left) and R=30 nm (right). The potential vanishes at a distance Ξ=22 nm far from the surface in both cases.*

can be measured through an Arrhenius plot (a measurement of the conductance under a slow change in sensor temperature). Thus, if the material and the environment are fixed, the potential Φ(r) and the surface-state density N_t can be determined as a function of the grain radius R.

The numerical solution of the model is reported, employing the experimental values for SnO_2 in air (T=400°C, ϵ=10^{-10}F/m, N_d=5×10^{18}cm^{-3} and V_s=0.68V). The Debye length is λ_D=2.7nm and the zero value of the potential is reached at a constant distance $\Xi \cong 8\lambda_D \cong$22nm from the surface, provided that R> Ξ.

The solution for R=100 nm and R=30 nm is shown in Fig. 1.6, which are typical values of different ranges of approximation: in the first case, R$\gg \Xi \gg \lambda_D$, thereby the depletion approximation under planar geometry would be sufficient to describe the situation; in the second case, R$\cong \Xi \cong \lambda_D$, thus the planar geometry cannot be used, but the depletion approximation still holds. The depletion approximation cannot be applied, when R becomes shorter than Ξ and the zero level cannot be reached. On the other hand, the model based on the complete charge density can be used in a wider range of grain radii since it does not have this intrinsic limitation. The example of grain radius R=10 nm is shown in Fig. 1.7: the potential does not have enough space to vanish.

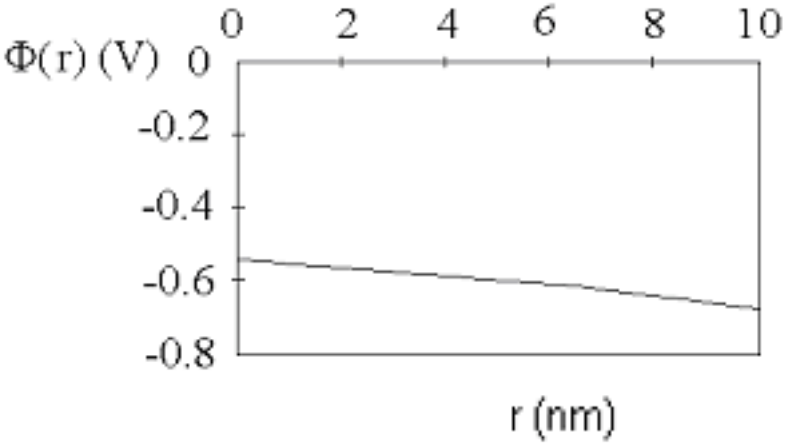

Figure 1.7: *Potential shape vs coordinate r for R=10 nm. The potential does not vanish even on the centre of the grain.*

1.3 Working mechanism models

A chemoresistive sensor is able to respond to an external stimulus (e.g., a gas concentration) with an electric signal (usually, a conductance change). Indeed, when a gas arrives at the surface of a sensor, it interacts both physically and chemically. Adsorption from the gaseous phase leads to charge exchanges between the adsorbate layer and the material itself, meaning a variation of the free electron concentration and, therefore, of the total number of electrons available for conduction. Many researchers have endeavoured to explain the basic mechanism of chemoresistive gas sensors. However, many aspects have not been deeply understood yet. In this section, the main sensing mechanism models will be described.

1.3.1 Conductance variation

Two kind of working processes can be distinguished for chemoresistive sensors [7]: the first one concerns bulk conducibility variations, the second one is connected to surface conducibility variations. Bulk conducibility variations are very important in oxygen partial pressure measurements. In this case, bulk chemical defects play a fundamental role, because the bulk has to be in equilibrium with atmospheric oxygen.

On the other hand, the second class of sensors is even able to detect different gases from oxygen. Indeed, the equilibrium value of surface conductance, which is reached in conditions of constant oxygen partial pressure, is influenced by the perturbing presence of surrounding gases. This class of sensors is sensitive to the variations of oxygen concentration too, but bulk chemical defects are less important for the measurements of atmospheric gases. The study of this second class of sensors will be mainly deepened. They are relatively simple and low-cost devices, consisting in a heater and a layer of a nanostructured semiconductor in contact with two electrodes, which are necessary to measure the conductance of the material. There are different ways to build the sensor, but two fundamental aspects still remain: the possibility of heating the device up to the desired temperature and of measuring the conductance. Metal oxides are the most suitable semiconductors in the implementation of this kind of sensors. In effect, while other kind of semiconductors may undergo irreversible chemical changes, after extended or cyclic heatings in ambient, creating stable layers of oxide, metal oxides bind surrounding oxygen in a reversible way.

The simplest and most common application of sensors consists in identifying a particular gas in the atmosphere, when there are not other kind of gases, that can generate a significant signal. However, an efficient and reliable device requires a certain selectivity, in order to detect and measure the presence of a single constituent in a random gas mixture. Selectivity can be obtained by adding catalysing elements, such as noble metals, to the semiconductor, even if, till now, the comprehension of the role of these dopants on the selectivity is not very deep and clear. Some general aspects were assigned for the functioning and employing of these materials in their different shapes, being single crystals, homogeneous thin films, porous thick films or partially syntherised grain layers [8]:

- the presence of oxygen is even necessary, in order to detect burner gases;
- as the temperature becomes higher, the sensitivity to a particular gas increases until it reaches a maximum value, afterward it decreases, approaching to zero for higher temperatures;
- the response in function of temperature is a logarithmic curve in a wide range of concentration, therefore low gas concentrations give an high differentiation, while this does not occur with greater concentrations;

- the response time to a rapid variation of concentration depends on both the nature of the gas and the working temperature; a quick starting response is often followed by a slower approach to the equilibrium (several hours in some cases);
- the response to burner gases is generally non selective;
- the presence of water vapour ponderously affects the response.

1.3.2 Conduction and morphology of the sensitive layer

Chemical reactions occurring on the surface are transduced to electric signals by means of the electrodes in contacts with the sensitive material. Reactions may occur at different points of the sensors, depending on its morphology. Two cases may be distinguished:

- compact and structurally homogeneous sensitive layer, in which the electron flow is parallel to the solid-gas interface, or even to the space charge layer; thus, the interaction with the gases occurs just on the top of the surface (see Fig. 1.9, such layer is obtained by most of the techniques used for thin film deposition);
- porous and not thin sensitive layer, made of partially sinterised grains, where electrons are forced to overcome the intergranular barrier; therefore, in this case, a certain thickness of material is available for reactions, because of the porosity, and the active surface is higher in comparison with the first case (see Fig. 1.10, such layer is typically a thick film).

A schematic representation of the two situations is depicted in Fig. 1.8 [11].

In the compact layer case, we may consider two different configurations: partially and completely depleted layer [11]. In the first case, when surface reactions do not influence the conductance of the whole layer ($z_g > z_0$ case, in Fig. 1.9), the conduction process takes place mainly in the bulk (z_g-z_0 thick), which turns out to be much more conductive than the depleted surface layer. This situation can be presented schematically with two parallel resistances: one influenced by surface reactions and the other not. Thus, the conduction is parallel to the surface and the reduced sensitivity is explained. The two configurations, partially and completely depleted layers, can switch one into the other, when in contact

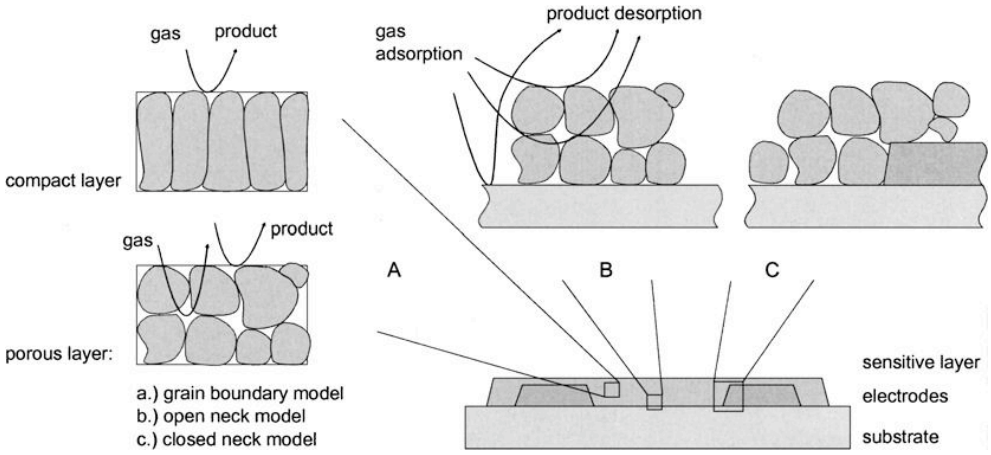

Figure 1.8: *Schematic layout of a typical resistive gas sensor. The sensitive metal oxide layer is deposited over the metal electrodes onto the substrate. In the case of compact layers, the gas cannot penetrate into the sensitive layer and the gas interaction is only taking place at the geometric surface. In the case of porous layers the gas penetrates into the sensitive layer down to the substrate. The gas interaction can therefore take place at the surface of individual grains, at grain-grain boundaries and at the interface between grains and electrodes and grains and substrates.*

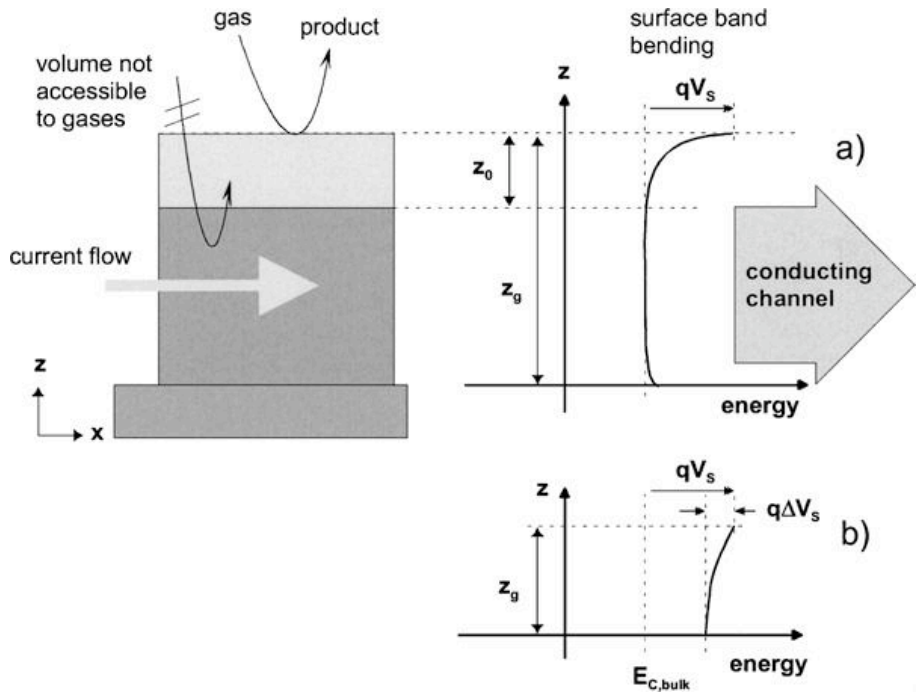

Figure 1.9: *Schematic depiction of a compact layer with geometry and energy band representations: the thicker partially depleted layer (a) and the thinner completely depleted layer (b).* z_0 *is the thickness of the depleted layer,* z_g *is the total thickness and* qV_S *is the band bending.*

with oxidizing and reducing gases, respectively, because withdrawal or injection of free charge carriers occur.

For porous layers, the presence of necks between grains (see Fig. 1.11) complicates the situation. Three contributions may be present in a porous layer: surface/bulk (for large enough necks, which corresponds to $z_n > z_0$ in Fig. 1.11), grain boundary (for large grains not sintered together) and flat bands (for small grains and small necks). The switching mentioned above for compact layers is also possible for porous ones.

In Fig. 1.10, we may observe the depletion area around grain surface and among intergranular contacts. The space charge region, depleted by charge carriers, is much more resistive than bulk, thus the layer close to the intergranular contacts is the main responsible for the resistance of the device. Considering the large grain model in Fig. 1.10, one notices that the charge carriers must overcome a potential barrier qV_S, in order to move from a grain to another. This means that the electric flow is limited by the density of

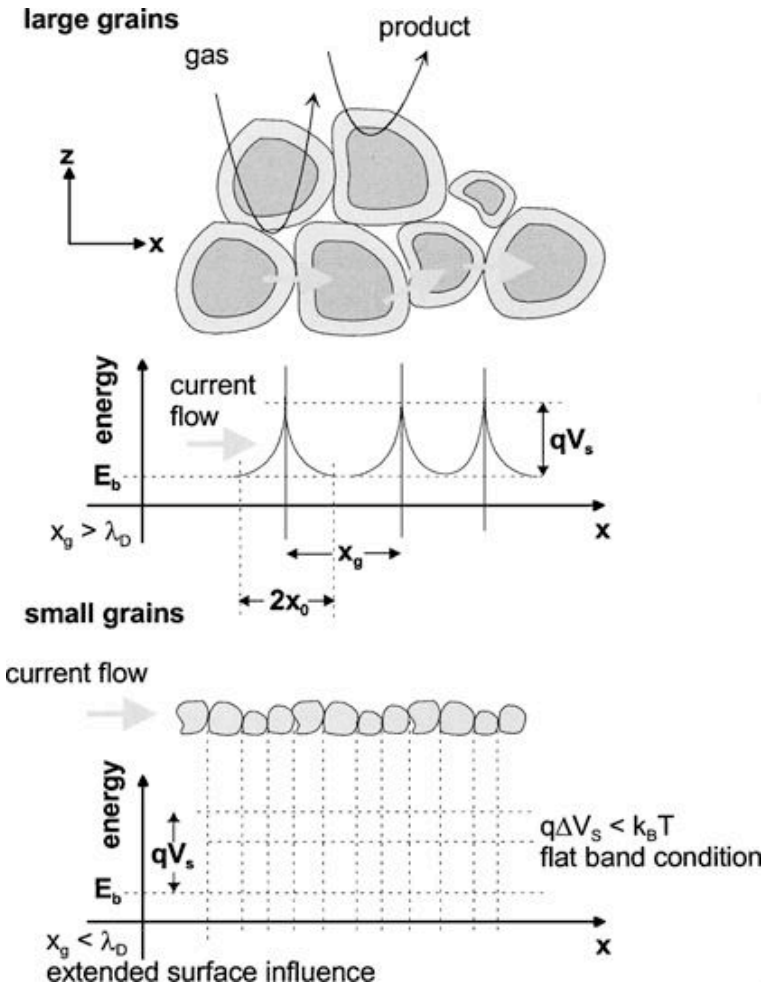

Figure 1.10: *Schematic depiction of a porous layer. λ_D is the Debye length and x_0 is the grain thickness.*

electrons with energy at least equals to:

$$n_S = N_C e^{-(qV_S + E_C - E_F)/kT} = N_D e^{-qV_S/kT} \tag{1.19}$$

where N_C represents the effective density of the states close to the bottom of the conduction band. Recalling Eq. 1.9, we may write:

$$n_S = N_D e^{q^2 N_S / 2\epsilon\epsilon_0 kT N_i} \tag{1.20}$$

In the end, oxygen atoms adsorbed on the surface capture electrons from the bulk of the material, leading to the formation of a considerable potential, V_S, which causes conduction variation, monitored for gas detection.

The intermediate case between compressed particle and thin films occur when particles are syntherised, as can be seen in Fig. 1.11. The formation of necks occurs between syntherised particles. The more the neck diameter grows, the more the control of material conductance is assumed by the necks, rather than the surface states. This effect happens when neck size is comparable to the thickness of the space charge layer, that is to say that the diameter of necks must be 10 nm as order of magnitude. Therefore, an accurate control of grain morphology is necessary, in order to have reliable sensors for their quantitative use in real conditions [12].

1.3.3 Effects of adsorbed gases on electric resistance of sensors

Metal-oxide semiconductors are employed as chemoresistive gas sensors, because their electric properties changes when gases interact with their surface. It is well-known that the electrical conductivity of metal oxides is dependent on gas adsorption. However, the interpretation of gas sensing mechanism is still controversial [13]. Two models have been proposed since now: the first one is based on *oxygen ionosorption*, while the second one on *oxygen vacancies*. Gas sensor response can be interpreted by both these mechanisms, which can be applicable at the same time [14].

At temperatures within 100°C and 500°C, the interaction between the surface of an n-type semiconductor, e.g. SnO_2, and atmospheric oxygen leads to its adsorption in the

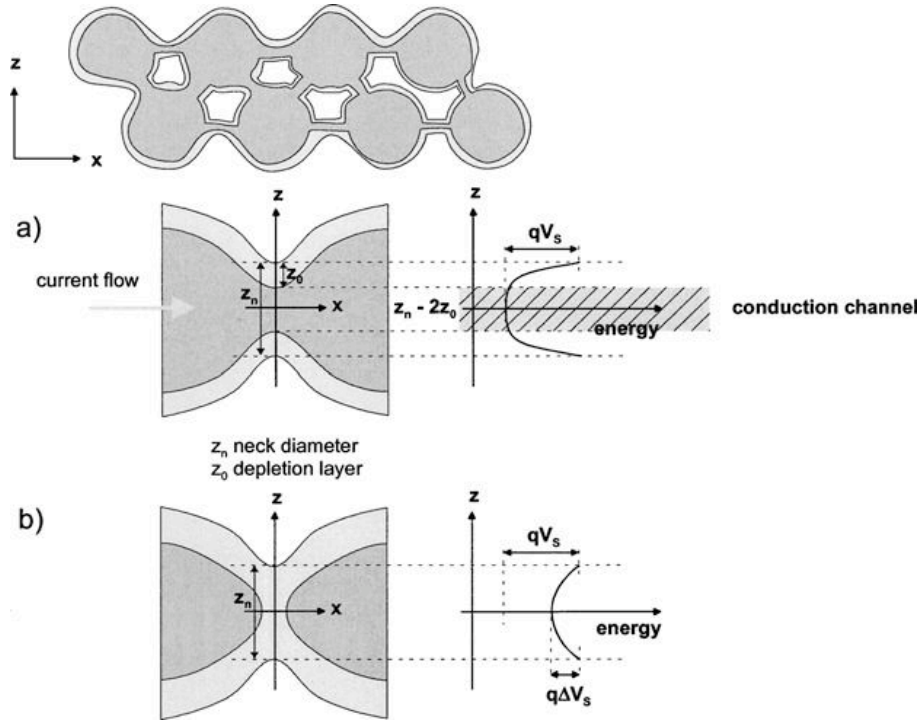

Figure 1.11: *Schematic depiction of a porous sensing layer with geometry and surface energy band-case with necks between grains: partially depleted neck (a) and completely depleted neck (b).* z_n *is the neck thickness and* z_0 *is depletion layer thickness.*

form of molecular (O_2^-) and atomic (O^- and O^{2-}) ions. Ionosorption does not envisage chemical bond: the adsorbate is electrostatically stabilised in the vicinity of the surface and acts as surface state, trapping electrons from the conduction band [7, 11, 14, 15]. Oxygen adsorption can be described by these simple reactions:

$$\begin{gathered} O_2(gas) + e^- \rightleftharpoons O_2^-(ads), \\ O_2^-(ads) + e^- \rightleftharpoons O_2^{2-}(ads) \rightleftharpoons 2O^-(ads) \end{gathered} \tag{1.21}$$

The molecular form is supposed to be dominant below 150°C, while above this temperature the atomic forms dominate [11]. However, we usually do not consider O^{2-}, because such a high charge on the ion can give instability, and O^- is reckoned to be as the most reactive species in presence of reducing gases [7].

The presence of adsorbed oxygen ions leads to the formation of a depletion layer at the surface of tin oxide and to a high resistance. When reducing gases, such as CO, approach the surface of the sensor, they react with the oxygen ions and release electrons, which return to the conduction band. The final effect will be a decrease of resistance and thus increase of sensor conductivity. In an oxygen-free atmosphere, CO acts as electron donor: it is adsorbed as CO^+ ion, thus releasing an electron in the conduction band [15]. Fig. 1.12 illustrate a scheme of ionosorption model.

The ionosorption model is widely accepted, even though is based mainly on phenomenological measurements and there is not yet any convincing spectroscopic evidence for ionosorbed oxygen species.

The oxygen-vacancy model is also consistent with most observations for semiconductor metal oxide gas sensors [14, 15, 16]. In this model, as suggested by its name, oxygen vacancies at the surface of tin oxide are the determining factor in the chemoresistive behaviour [16] and act as electron donors. Alternate reduction and reoxidation of the surface by gaseous oxygen (Mars-van Kravelen mechanism) control the surface conductivity and, therefore, the overall sensing behaviour. Three main steps can be specified: 1) CO removes oxygen from the surface of the lattice to give CO_2, thereby producing an oxygen vacancy; 2) the vacancy becomes ionized, thereby introducing electrons into the conduction band and increasing conductivity; 3) if oxygen is present, it fills the vacancy; in this proccess one or two electrons are taken from the conduction band, which results in the decrease in

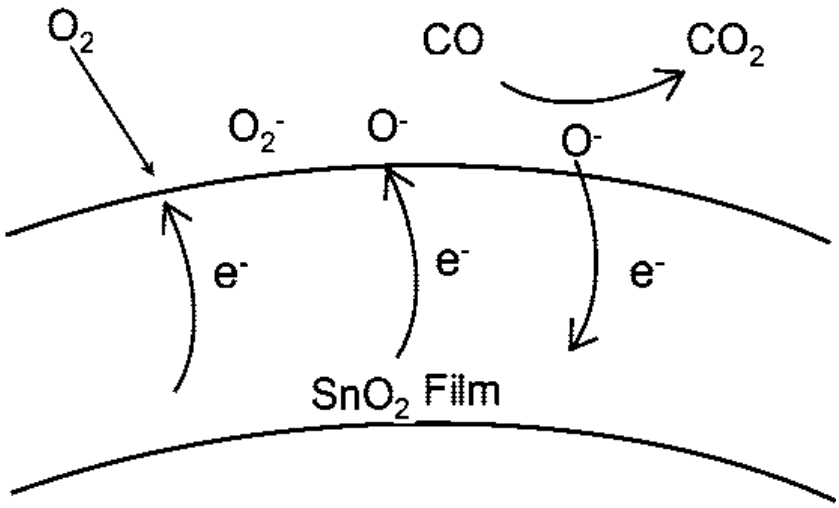

Figure 1.12: *Schematic depiction of ionosorption model for atmospheric O_2 interaction and CO gas sensing by SnO_2.*

conductivity. See Fig. 1.13 for a schematic depiction of this model.

The oxygen-vacancy model has not been discussed as widely as the ionosorption one, but numerous experimental and theoretical works have evaluated this explanation of gas-sensing effects, and it dominates in almost all spectroscopic studies.

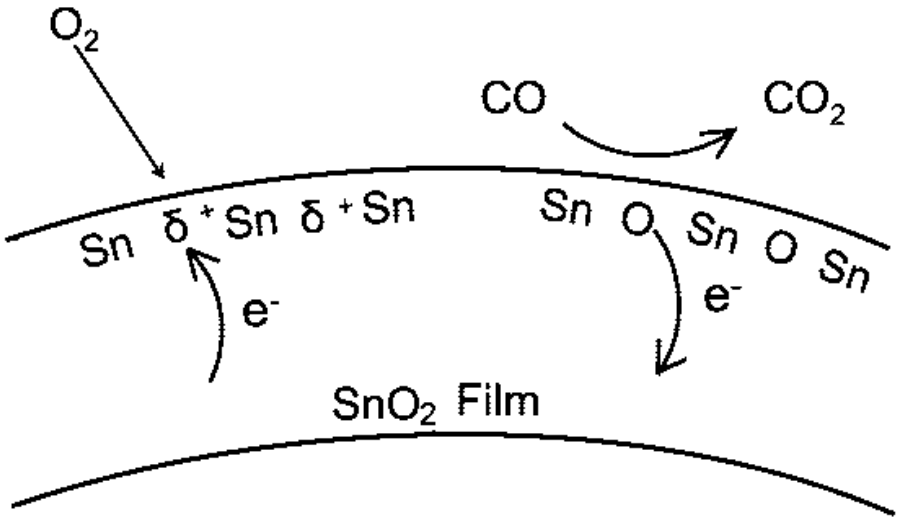

Figure 1.13: *Schematic depiction of oxygen-vacancy model for atmospheric O_2 interaction and CO gas sensing by SnO_2.*

Chapter 2

Gas adsorption processes

When a gas or vapour comes in contact with a clean solid surface, some of it will adhere to the surface in the form of an adsorbent layer. The solid is generally referred to as the *adsorbent*, the adsorbed gas or vapour as the *adsorbate*.

Any solid is capable of adsorbing a certain amount of gas. This quantity at equilibrium depends on the temperature, on the pressure of the gas and on the effective surface area of the solid. Therefore, the materials with the greatest adsorbent capacity are highly porous solids, such as charcoal and silica gel and finely divided powders. The relationship at a given temperature between the equilibrium amount of gas adsorbed and the pressure of the gas is known as the *adsorption isotherm*.

Adsorption reduces the imbalance of attractive forces which exists at a surface, and, hence, the surface free energy of a heterogeneous system.

2.1 Physisorption and chemisorption

Adsorption occurs when an attractive interaction between a gaseous particle and a solid surface is strong enough to overcome the disordering effect of thermal motion. *Physical adsorption* or *physisorption* takes place, if weak Van der Waals forces are involved in the interaction. Indeed, physisorptive bonds are characterised by dissociation energies below approximately 50 kJ/mol. Stronger forces are responsible for *chemisorption* and cause the formation of short chemical bonds with dissociation energies typically exceeding 50 kJ/mol.

Since an activation barrier needs often to be overcome, *chemisorption* is considered an activated process [17, 18].

From a thermodynamic point of view, adsorption is a spontaneous process, which means that the change in free energy of the system is negative. The change in entropy is negative, because the translational freedom of the adsorbate is reduced when it is adsorbed [19]. Therefore, considering the thermodynamic relationship:

$$\Delta G = \Delta H - T\Delta S < 0 \tag{2.1}$$

The enthalpy of adsorption, ΔH_{ads}, must be negative. Thus, the adsorption of gases on solids is an exothermic process. The extent of gas adsorption (under equilibrium conditions), therefore, increases with decreasing temperature. Exceptions may occur, if the adsorbate dissociates and has high translational mobility on the surface [19].

The equilibrium condition in physisorption is attained rapidly, since there is no activation energy involved and the process is readily reversible. On the other hand, chemisorption may require an activation energy, as already written, and may, therefore, be relatively slow and not readily reversible. Fig. 2.1 illustrates a schematic potential diagram for the adsorption of a diatomic molecule of gas, X_2, on a surface, M. Physisorption is described by a *Lennard-Jones* potential, whereas chemisorption by a *Morse* potential.

The physical interaction energy includes a short-range negative (attractive) contribution arising from London-Van der Waals dispersion forces and an even shorter-range positive contribution (Born repulsion) due to an overlapping of electron clouds. In chemisorption, the adsorbate, X_2, dissociates to 2X. The dissociation energy of X_2 (ΔE_{dis}) is represented at large distances. Both potential curves are characterised by the presence of a minimum, which corresponds to the heat of the process (ΔH_{ads}). The heat of chemisorption is at a shorter distance from the solid surface than the heat of physisorption.

A gas molecule is first physically adsorbed, which means that it approaches the solid surface along a low-energy path. The intersection point of the two curves represents the transition from physisorption to chemisorption, where the energy is the activation energy of chemisorption, ΔE_{ads}. The magnitude of this value depends on the shapes of the physical adsorption and chemisorption curves, thus it is variable according to the system [17].

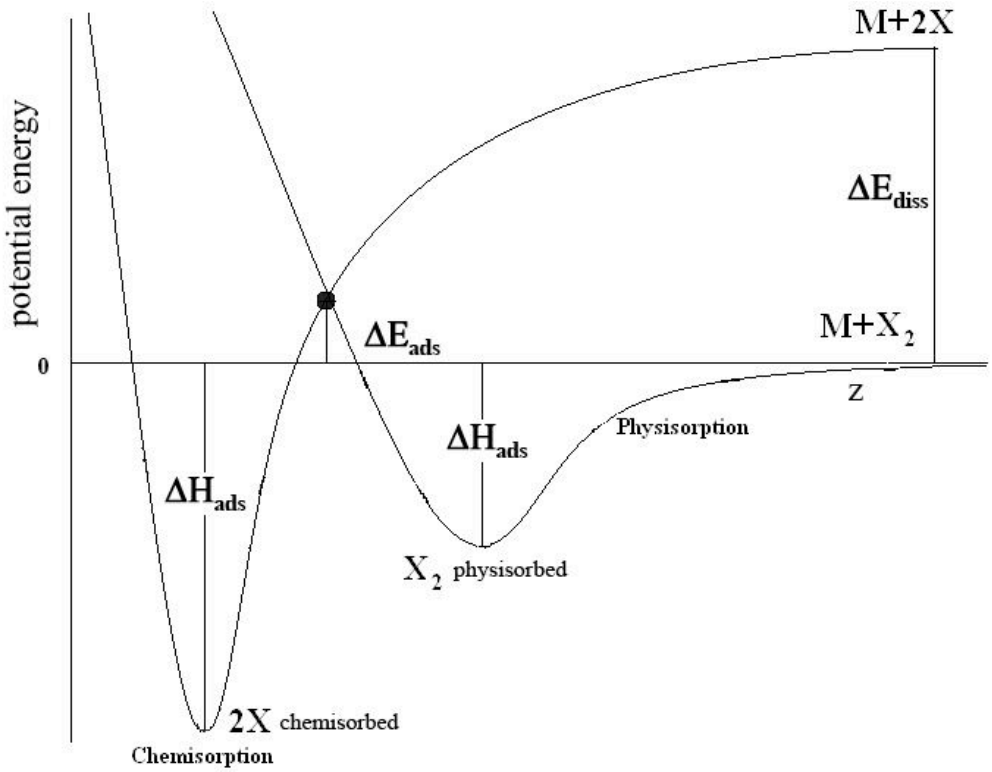

Figure 2.1: *Potential energy curves for physisorption and chemisorption of a molecule X_2 that approaches a surface along the trajectory z.*

2.2 Adsorption isotherms

The extent of surface coverage is expressed as a fractional coverage θ:

$$\theta = \frac{Number\ of\ adsorption\ sites\ occupied}{Number\ of\ adsorption\ sites\ available} \tag{2.2}$$

The change of fractional coverage with time $d\theta/dt$ determines the rate of surface coverage or *rate of adsorption*.

The fractional coverage θ is in equilibrium with the free overlying gas. This equilibrium, which is dynamic because generated by two opposite processes (adsorption and desorption) occurring at the same rate, depends on the pressure of the free gas and on the temperature of the system. The variation of θ with pressure at a chosen temperature is represented by a curve, called *adsorption isotherm*. This function has a particular importance in the determination of information about the active surface of a material, as it will be observed further on. Several adsorption isotherms[1] have proved to be useful in the understanding of the adsorption process. However, the three isotherm equations most frequently used are those due to *Langmuir*, to *Brunauer*, *Emmet* and *Teller* (*BET*) and to *Freundlich*.

2.2.1 The Langmuir isotherm

The Langmuir isotherm is based on the following characteristic assumptions:

- adsorption of a single layer (monolayer coverage);
- equivalence of all adsorption sites and surface uniformity;
- no interactions between adsorbed molecules.

We consider the dynamic equilibrium:
X(gas)+M(surface)$\rightleftharpoons$XM(surface)
The rate of adsorption is proportional to the partial pressure p of the gas X and to the

[1]Brunauer, Deming and Teller, based upon an extensive literature survey, found that all adsorption isotherms fit into five characteristic shapes, each reflecting some unique condition [20].

uncovered surface, expressed by (1-θ):

$$\frac{d\theta}{dt} = k_a p(1-\theta) \tag{2.3}$$

where k_a is the rate constant for adsorption.

The rate of desorption is proportional to the number of adsorbed species, represented by the surface coverage θ:

$$\frac{d\theta}{dt} = -k_d \theta \tag{2.4}$$

where k_d is the rate constant for desorption.

When adsorption equilibrium is established, θ is independent of time, thus both Eqs. 2.3 and 2.4 are equal. Solving this condition for θ, we obtain the *Langmuir isotherm*:

$$\theta = \frac{Kp}{1+Kp} \tag{2.5}$$

with $K = k_a/k_d$.

When considering a dissociative adsorption (X_2(gas)$\rightharpoonup$2X(surface)), the Langmuir isotherm has a different form. In this case, the rate of adsorption is proportional to the pressure and to the probability that both atoms will find sites, that is to say the square of the number of vacant sites:

$$\frac{d\theta}{dt} = k_a p(1-\theta)^2 \tag{2.6}$$

The rate of desorption is proportional to the frequency of encounters of atoms on the surface, thus proportional to the square of the number of atoms present:

$$\frac{d\theta}{dt} = -k_d \theta^2 \tag{2.7}$$

The equilibrium condition gives the following equation:

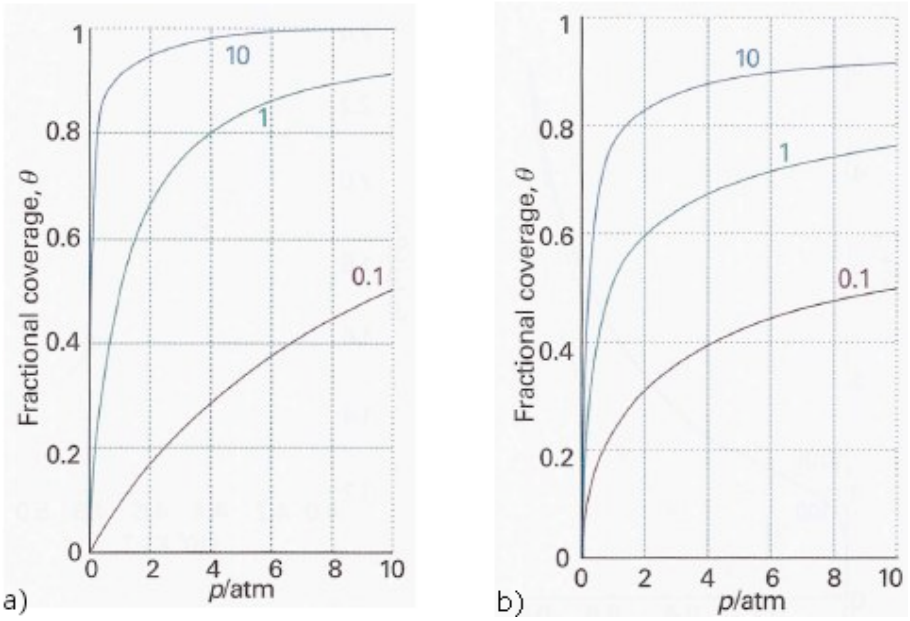

Figure 2.2: *Langmuir isotherms for dissociative (a) and non-dissociative (b) adsorption, for different values of K.*

$$\theta = \frac{(Kp)^{1/2}}{1 + (Kp)^{1/2}} \tag{2.8}$$

The dependence of θ on pressure is weaker than in the case of non-dissociative adsorption.

The trend of the Langmuir isotherms (see Figs. 2.2 for dissociative (a) and non-dissociative (b) adsorption, respectively) shows that the fractional coverage increases with increasing pressure and approaches one only at very high pressure, when the gas is forced on to every available site [19].

The value of the equilibrium constant K at various temperatures allows the determination of the *isosteric enthalpy of adsorption*, $\Delta H^{\ominus}_{ads}$, by means of the van't Hoff equation:

$$\left(\frac{\partial ln K}{\partial T}\right)_{\theta} = \frac{\Delta H^{\ominus}_{ads}}{RT^2} \tag{2.9}$$

2.2.2 The BET isotherm

The Langmuir isotherm is well applicable in the situation of low coverage, but it fails at high adsorbate pressure, thus high coverage. Therefore, another mathematical expression is necessary to predict the case in which the initial adsorbed layer acts as a substrate for further adsorptions (i.e., physisorption). Multilayer adsorption has been treated by Brunauer, Emmet and Teller, who gave the name to the corresponding isotherm. The derivation of this model stands on the balancing of the rates of evaporation and condensation for the various adsorbed molecular layers and on the assumption that a characteristic heat of adsorption $\Delta H^{\ominus}_{ads}$ applies for the first monolayer, while the heat of condensation $\Delta H^{\ominus}_{con}$ applies to adsorption in the second and subsequent molecular layers [17]. The BET isotherm is usually written in the form:

$$\frac{N}{N_{mon}} = \frac{W}{W_{mon}} = \frac{cz}{(1-z)1-(1-c)z} \tag{2.10}$$

with $z = p/p_0$, where p_0 is the vapour pressure above a layer of adsorbate (considered as a pure bulk liquid and thicker than a molecule). N and N_{mon} are the number of molecules in the incomplete and completed monolayer, respectively, and W/W_{mon} is the weight adsorbed relative to the weight adsorbed in a completed monolayer [20]. c is a constant depending on the extent of the enthalpy of adsorption compared to that of condensation:

$$c \propto e^{(\Delta H^{\ominus}_{con} - \Delta H^{\ominus}_{ads})/RT} \tag{2.11}$$

Since in multilayer coverage the vapour may condense to an unlimited extent, BET isotherms rise indefinitely as the pressure is increased, as shown in Fig. 2.3. The BET isotherm is reasonably valid over restricted pressure ranges, but it is not accurate at all values: it underestimate the extent of adsorption at low pressures and overestimates it at high pressures.

When $c \gg 1$, the BET isotherm takes the form:

$$\frac{N}{N_{mon}} = \frac{1}{1-z} \tag{2.12}$$

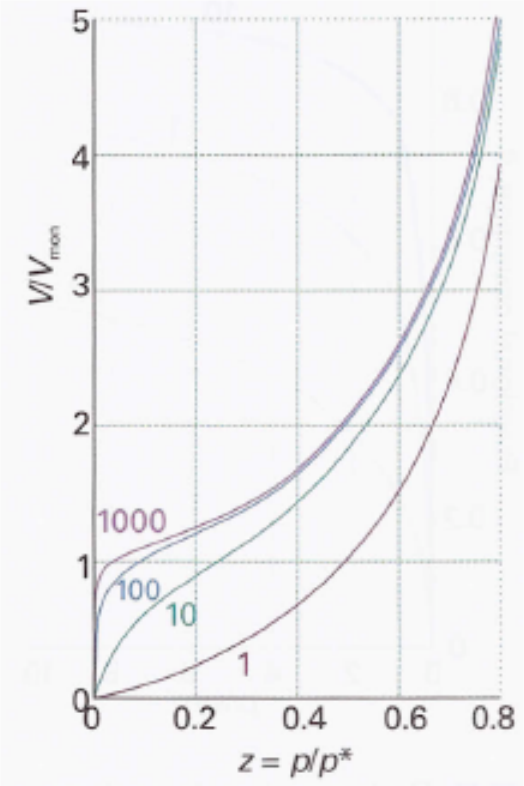

Figure 2.3: *BET isotherms for different values of c.*

This expression describes the case in which adsorption is stronger than condensation. It is usually applicable to unreactive gases on polar surfaces [19].

One of the main application of BET theory is the determination of the surface area of solids, as reported with more details in App. A.

2.2.3 The Freundlich isotherm

The change of adsorption with pressure can be represented by other equations, when deviations from the assumptions of the Langmuir model occur. The Freundlich isotherm corresponds to a logarithmic change:

$$\theta = c_1 p^{1/c_2} \tag{2.13}$$

where c_1 and c_2 are constants, c_2 usually being greater than unity.
Passing at the logarithms:

$$logV = logc_1 + 1/c_2 logp \tag{2.14}$$

Plotting $logV$ versus $logp$, the result should be a straight line. This adsorption equation is a good interpretation of an adsorption model in which the variation of the magnitude of the heat of adsorption with surface coverage is exponential. The Freundlich isotherm attempts to take into account the role of substrate-substrate interactions on the surface.

2.3 The rates of surface processes

Adsorption and its reversing mechanism, desorption, are characterised by a combination of elementary kinetic steps. We may assist to non-dissociative (a diatomic molecule is adsorbed on a surface) or dissociative (a diatomic molecule fragments into atoms adsorbed independently) processes, which are also known as first and second order kinetics, respectively [21].

The interaction of a gaseous molecule with a solid surface is shown in Fig. 2.4, where the potential energy profiles of a molecule undergoing dissociative and non-dissociative adsorptions are depicted. The energy of the molecule approaching the surface decreases until a minimum, at which the molecule is physisorbed. This step is considered a precursor state for chemisorption, which may occur with or without dissociation [19]. In both cases, the energy initially increases, as the distance from the surface decreases and the bonds stretch (in the dissociative process) or adjust (in the non-dissociative process); after that, a sharp decrease of the energy indicates that adsorbate-substrate bonds reach their full strength. A potential energy barrier separates the precursor and the chemisorbed states in case of dissociative chemisorption, because an energy input is required to fragment the molecule. Therefore, dissociative chemisorption is an activated process and is slower than the non-activated kind.

The rate at which a surface is covered by adsorbate depends on the ability of the substrate to dissipate the energy of the incoming particle as thermal motion, as it crashes on to the surface. If the dissipation of energy is not quick, the particle migrates over the

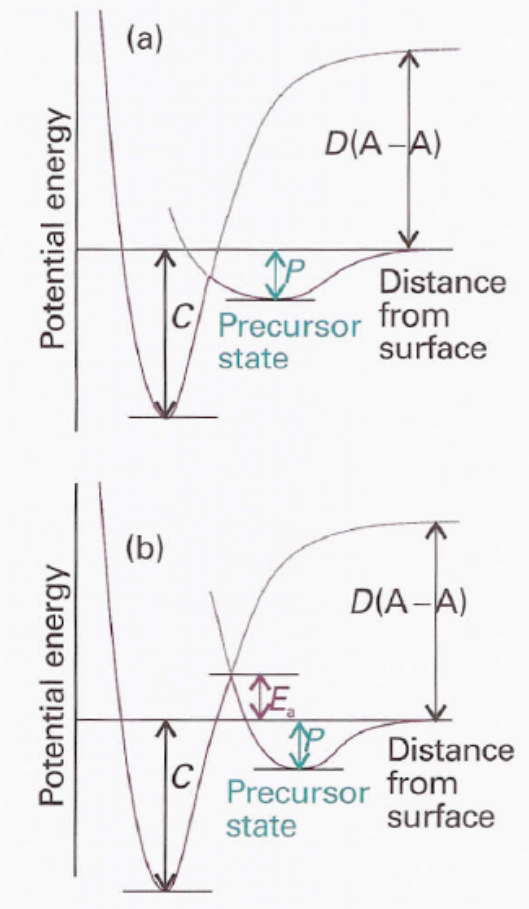

Figure 2.4: *Plots of potential energy versus distance for not activated (a) and activated (b) chemisorptions of a gaseous A_2 molecule. P is the enthalpy of physisorption, C that of chemisorption and E_a the activation energy for dissociative chemisorption.*

surface until it is expelled by a vibration into the overlying gas or it reaches an edge. The probability that gas molecules stick onto the surface, i.e. the proportion of collisions with the surface that successfully leads to adsorption is called the *sticking probability*, s:

$$s = \frac{rate\ of\ adsorption\ of\ particles\ by\ the\ surface}{rate\ of\ collision\ of\ particles\ with\ the\ surface} \tag{2.15}$$

The denominator can be derived from the kinetic model, and the numerator can be determined by observing the rate of change of the pressure.

The sticking probability varies widely and decreases as the surface coverage increases. A simple assumption is that the sticking probability is proportional to the fraction uncovered, 1-θ, and it is common to write:

$$s = (1 - \theta)s_0 \tag{2.16}$$

where s_0 is the sticking probability on a perfect clean surface (zero coverage)

As already mentioned at the beginning of this chapter, adsorption is an exothermic process, thus it ultimately yields energy (*energy of adsorption*), even if it requires some energy input (*activation energy*) to initiate. Reversing adsorption, desorption, is always an activated process, because it requires an input of energy, corresponding to the depth of the potential well.

Desorption involves the time rate of change of the fractional coverage $d\theta/dt$. This may also be viewed as the time rate change of the fraction uncovered, (1-θ).
The kinetic expressions for the rates of adsorption and desorption, expressed by Eqs. 2.6 and 2.7, can be written in a general way:

$$r_a(\theta) = \frac{d\theta}{dt} = k_a p(1 - \theta)^n \tag{2.17}$$

$$r_d(\theta) = -\frac{d\theta}{dt} = k_d \theta^n \tag{2.18}$$

where n is 1 and 2 for first and second order kinetics, respectively. This means that for

n=1 we have a first order rate law for adsorption and desorption, for n=2 we have a second order process, which corresponds to dissociative adsorption and recombinative desorption of diatomic molecules.

If the rate constant for desorption is described by the Arrhenius equation, with ν pre-exponential factor or desorption frequency factor,

$$k_d = \nu e^{(\frac{-E_{des}}{RT})} \tag{2.19}$$

then we obtain a new expression for the rate law of desorption, also known as the *Polanyi-Wigner* equation [18]:

$$r_d(\theta) = -\frac{d\theta}{dt} = \nu e^{(\frac{-E_{des}}{RT})}\theta^n \tag{2.20}$$

which is very useful in the determination of the activation energy of desorption, as it will be discussed in Ch. 4.

Chapter 3

Synthesis and deposition techniques

3.1 Synthesis of the nanostructured metal-oxide powders

The sensitive materials used in the preparation of the chemoresistive gas sensors require specific characteristics. Since interactions with the gas phase occur on the surface, precisely just below the solid-gas interface, a high specific surface area represents the first requirement, in order to enhance the sensitivity of the material. Therefore, the sensitive powder must be composed of nanometric grains (with mean radius of tens nm). The synthesis of metal-oxide powders is, thus, an important and delicate step of the whole process of sensor production.

The sol-gel technique was used for the preparation of the powders. Sol-gel is one of the most used method to synthesise a great variety of inorganic networks, employing silicon or other metal alkoxides as precursors. It is possible to prepare, at relatively low temperatures, materials based on inorganic oxides with the desired characteristics (hardness, chemical resistance, porosity and thermal resistance). The process consists mainly of three steps: it involves the hydrolysis of the organic precursor solution, the formation of a colloidal suspension and its evolution into a gel through condensation [22]. The structure of the final gel may differ, according to the variation of certain parameters, such as reaction temperature, water ratio and pH (acid or basic catalysis).

The precursor for the preparation of SnO_2 is tin(II)2-ethylexanoate. A given amount of

deionized water is added drop-wise to an n-butanol solution 0.7 M of tin(II)2-ethylexanoate, stirring it at room temperature for 3 h. The molar ratio of water to Sn is 4 and the pH of the solution is set at the unity with HNO_3. The resulting gel is dried at 95°C for 12 h in order to obtain a yellow powder, which is subsequently calcined at 550°C for 2 h [33].

Titanium butoxide (TB) is used as a source of titanium to synthesise the TiO_2. TB dissolved in the absolute ethanol (0.23 M) is added drop by drop to a solution of ethanol/water 1:1 vol under mild stirring. This step is followed by 20 min of vigorous stirring. The obtained suspension is treated by means of the sol-gel process. After stirring, 16 h resting followed, the suspension was filtered to obtain a white precipitate, which is dried in air (100°C) for 16 h. Finally, the powders are calcined at 400°C in air for 2 h [34].

The solid solutions of Sn and Ti mixed oxide are produced via symplectic gel coprecipitation (SGC) of stoichiometric Sn(4+) and Ti(4+) hydroalcoholic solutions and further calcination of the resulting xerogels. Calcination is performed at 550°C for 2 h under air-flow condition. The nanocrystalline powders obtained have a particle-size distribution which averages about 20nm, as determined by SEM [35]. The solid solutions of $Ti_xSn_{1-x}O_2$ with different values of x (x=0.1, 0.3, 0.5, 0.7 and 0.9) will be hereinafter labeled as ST10, ST30, ST50, ST70 and ST90 [35]. Nb is added to the pure solution of $Sn_{0.7}Ti_{0.3}O_2$ (ST30) by coprecipitation, in the proportion of Sn:Ti:Nb=100:42:5 in order to enhance the conductivity. The resulting powder, named STN, is calcined at 400°C for 2h.

3.2 The serigraphic process

Thick film technology, also known as serigraphic technology, is a wide-used manufacturing method, which differs from others for the film deposition process [23, 24]. It was introduced about thirty years ago in the production of hybrid circuits. Since then, many are the fields of application for this technology, e.g. television sets, computers, mobiles, electronics for automotive industry. Thick film hybrid circuits are characterised by well known qualities, such as compactness, hardness and relatively low cost compared to other technologies. Thick film technology has been recently applied to the sensing field, both for the passive electronic components and for the sensors.

The serigraphic technology has widely developed over the last twenty years, mainly for

three aspects.

- *width of the deposition*, thanks to the substitution of traditional masks into new ones made of steel and obtained by means of a laser, leading to films characterised by a minimum width of 20 μm;
- *serigraphic pastes*, whose improvement relies on the realisation of a great quantity of sensors, based on different functional materials;
- *miniaturisation* and compactness of the planar structures of thick films and multilayer configurations were recongnised to be appealing characteristics in the sensing field.

However, the combination of the mass production capability to a relatively low cost (in comparison with other technologies) and the reliability of devices in difficult operating conditions make planar thick film technology one of the most suitable for sensors with the following requiremments:

- sensitivity to low pollutant concentrations;
- reliability;
- repeatability;
- low energetic consumption;
- moderate sizes;
- low ratio cost/performance;
- automation possibility.

3.3 Production process of thick films

This section comprises the description of the main steps necessary to prepare thick films by means of the serigraphic technology. Some variations were performed in the Sensor and Semiconductor Laboratory of Ferrara, in order to obtain sensors well suitable for specific detecting demands. First of all, it must be underlined that the method employed

Figure 3.1: *Serigraphic machine equipped of a camera positioning system, operating in a clean room in order to avoid defects during deposition.*

allows the deposition on the same substrate, not only of the sensitive film, but also of the heating elements, the interdigitated contacts and the elements necessary to the control of the sensor operating temperature. The serigraphic machine employed in the Sensor and Semiconductor Laboratory is shown in Fig. 3.1.

The employed substrates are made of laser pre-cut ceramic material: each element is a 0.25 mm-thick-2×2 mm^2 square. The advanced technology of the serigraphic-deposition apparatus, equipped of cameras and electronic control for the positioning of the substrate during the multilayer configuration steps (see Fig. 3.2), allows the manufacturing of hundreds of sensors at a time.

The deposition of the passive electronic components (conductors, resistors and dielectrics) is performed by means of commercial pastes, while the gas sensitive layers are produced through the serigraphic pastes and the functional material powders prepared by

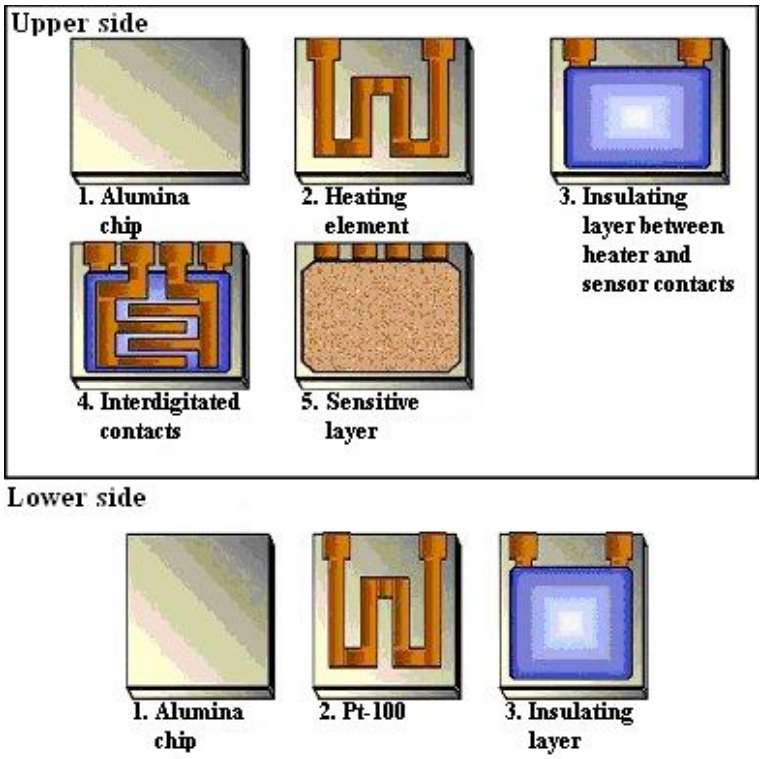

Figure 3.2: *Multilayer configuration of the sensor. On the upper side, the sensitive layer is deposited among the comb contacts and represents an electric circuit lock. The self-adjusting temperature system, which consists of a variable resistor (Pt-100), is shown on the lower side.*

the sol-gel technique, as already described (see Par. 3.1).

3.3.1 Preparation of the pastes

The *functional phase* is formed by:

- metal-oxide or semiconductor powder in case of resistive pastes;
- metal or metal-oxide powder for the preparation of conductors;
- vitreous or ceramic powder for the dielectric compositions.

The *binder* consists of a vitreous powder and has the function to promote film adhesion to the substrate after thermal treatment. The *vehicle* is a mixture of a resin and a volatile

solvent (*medium*) with the temporary binder function.

The ability to detect a few ppm of gas is assured by the fact that the functional material of the sensitive layer is made up of nanostructered metal-oxide powders, which control the electric and sensitive properties of the film. Indeed, the decrease of the particle size, from a micrometer order of magnitude to a nanometer one, emphasises important changes in the physical properties, which, in our case, comprise the interaction between film particles and gas molecules. Moreover, the highest ratio between surface and volume in nanometric materials makes surface properties become more important. Thus, these materials results to be particularly suitable for the detection of gas traces. Therefore, an accurate synthesis of those powders represents an important step in the preparation of the sensing film, taking into account many factors, such as shape and size of grains, their homogeneity, intergranular porosity and surface conditions [25, 26, 27].

Following the synthesis of the powders is the printing of the sensitive layer. This phase requires the preparation of a viscous paste, which is obtained adding an organic vehicle, consisting of a mixture of rheological agents (usually a resin made up of α-terpineol and ethyl-cellulose) in volatile solvents (for instance, 2(2-butoxyethoxy)ethyl acetate), to the nanometric powder. The composition of the organic vehicle gives printability to the paste, electrical and macroscopic morphological characteristics to the fired film. This ingredient is completely removed during the thermal processes, during which we assist to the formation of the microstructure of the deposited film. There is also a third constituent in the paste: a small quantity of inorganic binding agent, vitreous powders, helping the adhesion of the film to the substrate, and metal oxides, promoting the interdiffusion of particles during firing. On the whole, the preparation of the paste is a delicate step, because of the complexity of the system, which requires a certain number of components and involves specific phenomena in order to transform the deposited layers into functional films.

3.3.2 Substrates

The substrates are the physical support of the thick film layer, with which they form a single structure. Their role is to assure a suitable electric insulation for the circuit components and to provide for the dissipation of the Joule-effect heat. One of the most

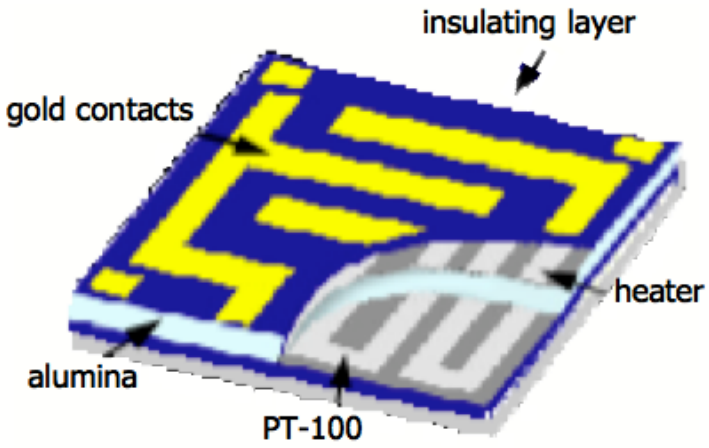

Figure 3.3: *Scheme of the substrate, composed of its elements and layers.*

employed substrate in thick film technology is alumina (96% Al_2O_3). A scheme of the substrate is depicted in Fig. 3.3.

3.3.3 Printing

Printing on alumina substrates represents a fundamental step in the manufacturing process. This part of the process is performed by means of extrusion of the paste through the meshes of a screen (see Fig. 3.4. The paste is forced to go out, because of the decrease of viscosity caused by the pressure of the rubber-blade, which crosses the screen at a certain rate. The deposited layer may vary in a range of few up to 100 μm and depends on the following parameters:

- particle size;
- paste viscosity;
- mesh number of the screen;
- strain of the steel threads that form the screen ;
- rubber-blade hardness;

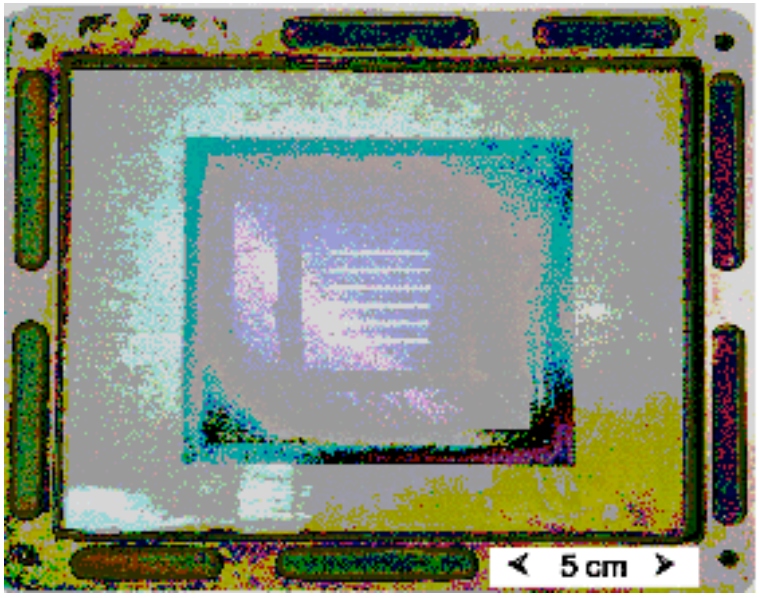

Figure 3.4: *Serigraphic screen, containing the substrates of alumina, where the deposition of the sensitive layers occurs. The frame must be projected in order to avoid deformations. The case depicted in this figure is characterised by a 20 N/cm strain and 300 meshes. The thread has a 18 μm diameter and the emulsion 25 μm. The minimum width for one line and for the resolution between adjacent lines is 100 μm order of magnitude.*

- rubber-blade velocity;
- distance between screen and substrate (snap-off).

3.3.4 Drying up

The drying up of the deposited layer is performed in a clean environment, in a oven at about 200°C. It promotes the evaporation of the vehicle volatile components. Thus, the films appears solid and sticks to the substrate.

3.3.5 Sinterisation

Sinterisation consists in a firing in free or control atmosphere. This process is necessary to remove the left organic vehicle, so that the layer becomes all-in-one with the substrate.

A steady, definite and stable structure is, thus, obtained. Firing usually occurs in air, inside a muffle furnace, following temperature ramps suitable for each kind of sensor. Maximum temperature ranges from 600°C up to 900°C, according to the desired electrical and microstructural characteristics.

Chapter 4

Temperature-programmed desorption measurements

Temperature-programmed desorption techniques are useful methods for the determination of kinetic and thermodynamic parameters of desorption processes. As the name of the method implies, the effects of temperature on surface reactions are involved. A sample is pre-treated to remove any adsorbed species from the active surface. Then, a gas is chemisorbed onto the active sites until saturation is achieved. After this first phase, the sample is heated with a temperature programme $\beta(t)=dT/dt$ (with the temperature T usually being a linear function of the time t) and the signal corresponding to the atoms and molecules evolving from the sample is measured, e.g. by a mass spectrometer.

Temperature-programmed desorption (TPD) and *intermittent temperature-programmed desorption* (ITPD) turned out to be powerful characterising techniques for chemoresistive materials applied to gas sensing. ITPD is a differential form of TPD where a sequence of interrupted desorption runs is generated by means of a saw-tooth heating programme. It is an improved and well tested technique [28, 29], whose advantage consists in deducing the activation energy values in a simpler way compared to a single TPD profile.

4.1 Theoretical model

Physical models of TPD are most often based upon a mass balance on the adsorption cell at quasi-steady state.

Recalling the Polanyi-Wigner equation for the rate law of desorption of kinetic order n (Eq. 2.20), we can write another expression, adding an adsorption contribution which takes into account the case of free readsorption [30]:

$$-\frac{d\theta}{dt} = \nu\theta^n e^{(-E_{des}/RT)} - \mu(1-\theta)^n p e^{(-E_{ads}/RT)} \tag{4.1}$$

where μ is the preexponential factor of adsorption rate expressed in reciprocal pressure units, as frequently used for gases.

When a desorption experiment is performed under vacuum, the accumulation of the gas in the adsorption cell is considered negligible. Thus, the mass balance over the sample cell is defined by the following equation:

$$-q_m\frac{d\theta}{dt} = Cp \tag{4.2}$$

where q_m is the amount of gas adsorbed at saturation, p is the pressure of the gas above the sample and C is the conductivity of the tube connecting the sample cell to the vacuum system ($C = \frac{\pi^{3/2}}{8\sqrt{2}}\frac{D^3}{L}\sqrt{\frac{RT}{M}}$, where D and L represent the inner diameter of the tube and its equivalent length, respectively, M denotes the molar mass of the gas and T is the room temperature). A similar expression can be written for experiments carried out under an inert gas stream:

$$-q_m\frac{d\theta}{dt} = Fp \tag{4.3}$$

where F represents the total volumetric flow through the desorption cell.

Getting the pressure p from Eq. 4.2 or 4.3 and replacing it into Eq. 4.1, then the neat desorption rate is obtained:

$$-q_m\frac{d\theta}{dt}=\frac{q_m\nu\theta^n e^{(-E_{des}/RT)}}{1+\frac{q_m\mu}{X}(1-\theta)^n e^{(-E_{ads}/RT)}} \tag{4.4}$$

where X represents either C or F, according to the experimental case.

If free readsorption does not occur, the second term in the denominator of Eq. 4.4 is much smaller than 1 and the equation becomes:

$$-\frac{d\theta}{dt}=\nu\theta^n e^{(-E_{des}/RT)} \tag{4.5}$$

In this case, the energy E (obtained at quasi-constant coverage) is equal to the activation energy of desorption, E_{des}.

In the case of free readsorption, on the other hand, the second term is much larger than 1, so that another expression is obtained:

$$-q_m\frac{d\theta}{dt}=\frac{X\nu}{\mu}(\frac{\theta}{1-\theta})^n e^{(\Delta H/RT)} \tag{4.6}$$

where $\Delta H=E_{ads}-E_{des}$ [30]. In this case, E is equal to $-\Delta H$.

Another way of writing Eq. 4.5 and 4.6 results useful, when calculating the preexponantional factor:

$$-\frac{d\theta}{dt}=Ae^{(-E/RT)}f(\theta) \tag{4.7}$$

where, without readsorption, $A=\nu$ and $f(\theta)=\theta^n$; while in the case of free readsorption, $A=\frac{C\nu}{\mu q_m}$ and $f(\theta)=(\frac{\theta}{1-\theta})^n$ [31].

The preexponential factor, also called *frequency factor*, is of great interest, when discussing desorption experimental results (see Par. 4.3). We refer to the apparent energy of desorption, E_{app}, when considering the experimental value, without knowing wether readsorption occurs or not. The related apparent frequency factor, A_{app}, can be obtained using the following equation [29]:

$$A_{app} = \frac{1}{N_{tot}} \frac{dN}{dt} exp \frac{E_{app}}{RT} \tag{4.8}$$

where N is the amount of adsorbed species in a given state and N_{tot} is the amount of gas necessary to saturate the considered state. N_{tot} and dN/dt are experimentally available from the cumulative area of partial TPDs (when ITPD runs are performed) corresponding to the given state and from the measured desorption rate at the temperature T, respectively [32].

4.2 TPD and ITPD experiment

TPD and ITPD experiments were performed at *IRCELYON* (*Institut de Recherches sur la Catalyse et l'Environnement de Lyon*). Samples of SnO_2, TiO_2 and solid solutions of them ($Ti_xSn_{1-x}O_2$) were employed, in order to obtain information concerning their surface properties. All the samples were prepared by the sol-gel method (see 3.1), except for SnO_2 which was a commercial powder (CERAC). Specific surface areas of the samples were measured according to the BET method by nitrogen adsorption at 77 K with samples previously evacuated at 300°C under 10^{-1} mbar for 2.5 h. A Micromeritics TRISTAR 3000 was used for the purpose (see App. A for further details). Specific surface area values ranged from 8 to 115 $m^2 \cdot g^{-1}$ (see Tab. 4.1).

Table 4.1: Specific Surface Area values.

Sample	*Mass* (g)	*Specific Surface Area* (m^2/g)
$ST30$	0.1488	85.7544 ± 0.7808
$ST50$	0.1670	106.0993 ± 0.7302
$ST70$	0.1523	89.8188 ± 1.1113
SnO_2	0.4299	8.2468 ± 0.0428
TiO_2	0.0851	114.9866 ± 0.8358

Figure 4.1: *Picture of the experimental setup for vacuum TPD and ITPD.*

4.2.1 Experimental apparatus

The experimental apparatus used for TPD and ITPD runs is a laboratory-built set-up schematically described in Fig. 4.1.

The sample (about 100 mg) was located in a cylindrical stainless steel sample holder (50 mm height and 4.0 mm in inner diameter) hanged in vacuum by K-type thermocouple wires (50 μm in diameter, spot-welded onto the sample holder) in the centre of a cylindrical quartz reactor. The powder was heated by means of a high-frequency system (1.1 MHz, 6 kW, manufactured by CFEI, France) with a 6-turn inductive coil placed around the reactor. A fast heating is assured with a small temperature gradient. Therefore, the sample holder is virtually thermally (except radiation mode) and mechanically isolated from both the reactor and the heating device.

The reactor can be evacuated down to $5{\cdot}10^{-8}$ mbar by a turbomolecular pump and the mass spectrometer is fitted with its own pumping system down to $1{\cdot}10^{-7}$ mbar. Analysis of species released during desorption runs was carried out by a quadrupole mass spectrometer (Vggas Smart-IQ+).

4.2.2 Description of the experiments

Each sample was first evacuated down to $1{\cdot}10^{-6}$ mbar at room temperature and then heated at 20 K·min^{-1} from room temperature up to 500°C in pure O_2 under 133 mbar. After the desired adsorption time (30 min), the sample holder was cooled down to room temperature under O_2 and then evacuated to 10^{-6} mbar. After that, the reactor was isolated from the vacuum line and directly connected to the MS through a large diameter UHV valve. The evacuation of the reactor was continued using a turbo molecular pump of the MS and the signals corresponding to the evacuated species were followed by the MS. The repetition of this procedure before each run insures that TPD runs were started at a nearly constant value of the oxygen-related MS signal corresponding to roughly 10^{-6} mbar in the reactor. The TPD experiments were performed heating at 20 K·min^{-1}. Desorbed molecules were detected from room temperature to 850°C, following the mass peaks at m/e=16, 18, 28, 32, and 44 amu. After TPD runs, samples ST30 and ST50 were chosen for ITPD experiments, which consisted in "slicing" the complete TPD profile by means of a saw-tooth heating programmme. Temperature was increased to create oxygen partial TPDs, which were interrupted by temperature decreases. The heating rate of the ascendant part was 20 K·min^{-1}. During the descendant parts, the sample was allowed to cool at a higher rate in order to get the MS signal at m/e=32 back to its initial background level. Desorption was intermittent in this process.

4.3 Results and discussion

Two successive TPD runs were performed for each sample. Between the two runs, sample was allowed to cool down freely at 500°C and then was submitted to the adsorption procedure described above, before undergoing the second TPD run. As shown in Fig. 4.2 for ST50 sample the first TPD profile is more governed by desorption of contaminants arising either from elaboration process or from storage in ambient atmosphere. A similar observation was made for ST30 and ST70 samples. These species, mainly CO/CO_2 certainly arising from some carbonates decomposition, and water are far much abundant than O_2,

the desorption of which is detected in the 400-850°C range. Indeed, water and carbonates are very stable species under O_2 at 500°C and block oxygen adsorption sites. Therefore, as shown in Fig. 4.3, after the first desorption the surface was cleaned and more oxygen was adsorbed and desorbed during the second TPD run. Moreover, as oxides have to be fired at high temperature (in the 600-800°C range) during the process to obtain the final sensing layer, it is evident that the first TPD is not representative at all of the properties of the material of interest. Therefore, only data from the second TPD were considered and corresponding profiles for samples SnO_2, ST30, ST50, ST70, and TiO2 are shown in Fig. 4.4. As one can notice, the SnO_2 spectrum is characterised by the highest amount of desorbed O_2 with a composite desorption peak with maxima at about 570 and 730°C, in agreement with literature data [36, 37], while TiO_2 seems to be the less performing powder concerning the amount of released dioxygen. For STx samples, the amount of desorbed dioxygen increases when the amount of SnO_2 in the mixed oxide increases (decrease of x). Corresponding quantitative data are given in Tab. 4.2 and they also show that the amounts of oxygen species desorbed from sample STx are lower than those desorbed from SnO_2, but do not correspond to a mere linear combination of (1-x)SnO_2 / xTiO_2. This indicates the formation of a mixed oxide with different properties from both SnO_2 and TiO_2. This conclusion is also supported by the shape of O_2-TPD profiles from STx samples which are quite different from those of the Sn and Ti oxides. Except for SnO_2 sample, the desorbed oxygen amounts represent less than 10% of a compact monolayer of ions O_2^- (corresponding to a theoretical maximal coverage of 13.7 μmol O_2/m^2 [38]). This result excludes that oxygen is significantly desorbing from the bulk and indicates the presence of surface species, which play an important role in the solid-gas interactions.

Table 4.2: O_2 desorbed quantities after the second TPD run.

Sample	*Mass* (*g*)	*Desorbed* O_2 ($\mu mol/m^2$)
*ST*30	0.0986	0.20
*ST*50	0.0947	0.10
*ST*70	0.1374	0.06
SnO_2	0.1368	1.98
TiO_2	0.13661	0.04

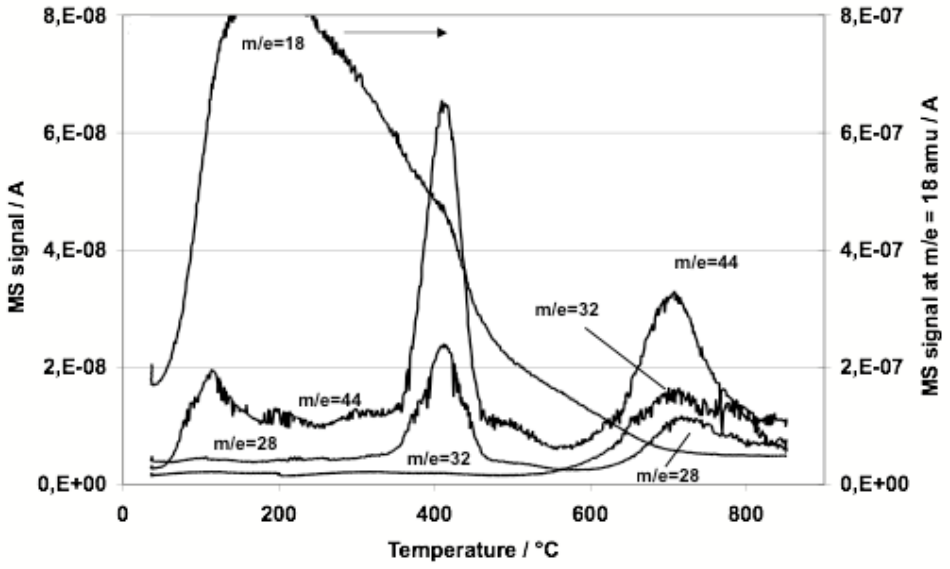

Figure 4.2: *TPD profiles (signals at m/e = 18, 28, 32 and 44 amu) of the ST50 sample after the first O_2 adsorption at 500°C.*

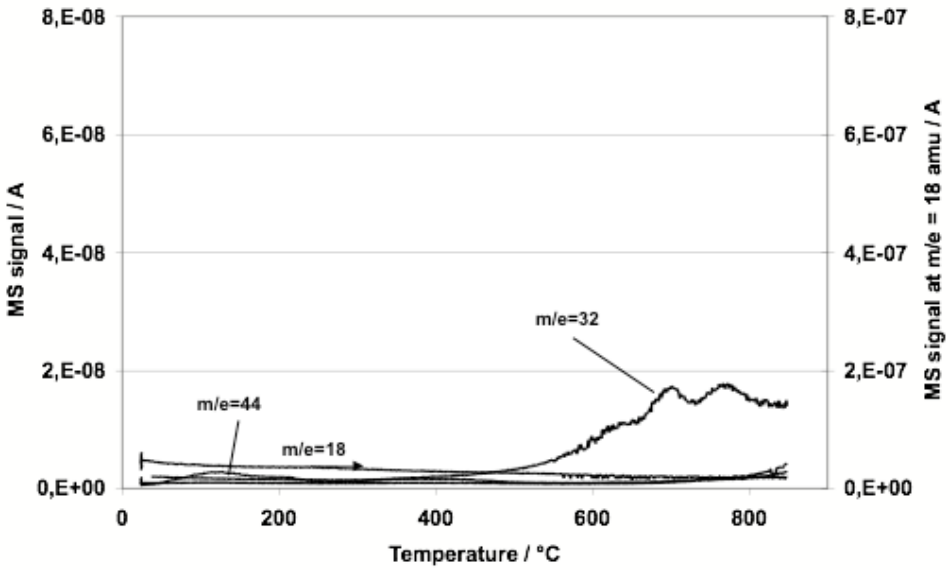

Figure 4.3: *TPD profiles (signals at m/e = 18, 28, 32 and 44 amu) of the ST50 sample after the second O_2 adsorption at 50°C.*

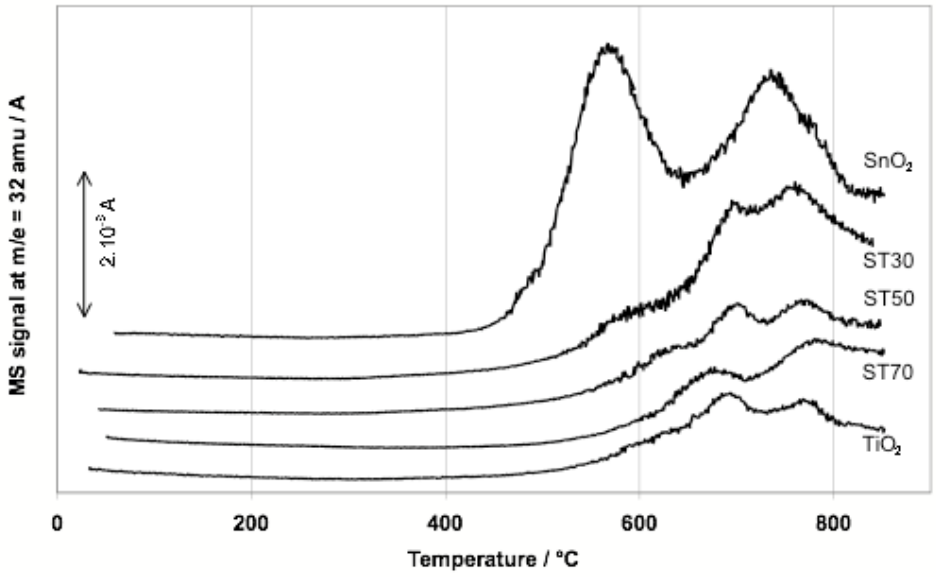

Figure 4.4: *Complete O_2-TPD profiles of the samples after the second O_2 adsorption at 500°C (traces are offset to improve readability).*

The apparent activation energy of desorption E_{app} and the associated frequency factors A_{app} corresponding to each adsorption state can be obtained by fitting the experimental TPD profile (more precisely, a set of classical TPD first order or second order model peaks). However, such an approach is not reliable and an investigation by ITPD was preferred. The ITPD procedure may be better understood considering Fig. 4.5, where the heating programme and the corresponding series of partial desorption curves (MS signal at m/e = 32) are shown for ST50 sample submitted to oxygen adsorption at 500°C. To check for the reliability of the experiment, the sum of the area under each partial TPD was compared to the total area under the TPD curve presented in Fig. 4.4. The calculated values $1.9{\cdot}10^{-7}$ and $1.7{\cdot}10^{-7}$ A.s.mg$_{sample^{-1}}$ for TPD and ITPD, respectively, are in satisfactory agreement. The variation of MS signal at 32 amu versus temperature for ST50 sample is shown in Fig. 4.6 for the 21 partial TPDs, restricted to their ascending part in order to improve readability. The complete corresponding TPD is also shown on the same plot, in order to allow the localisation of four distinct zones corresponding to shoulder or peaks and labelled, α, β, γ, and δ, according to their order of appearance when temperature

increases.

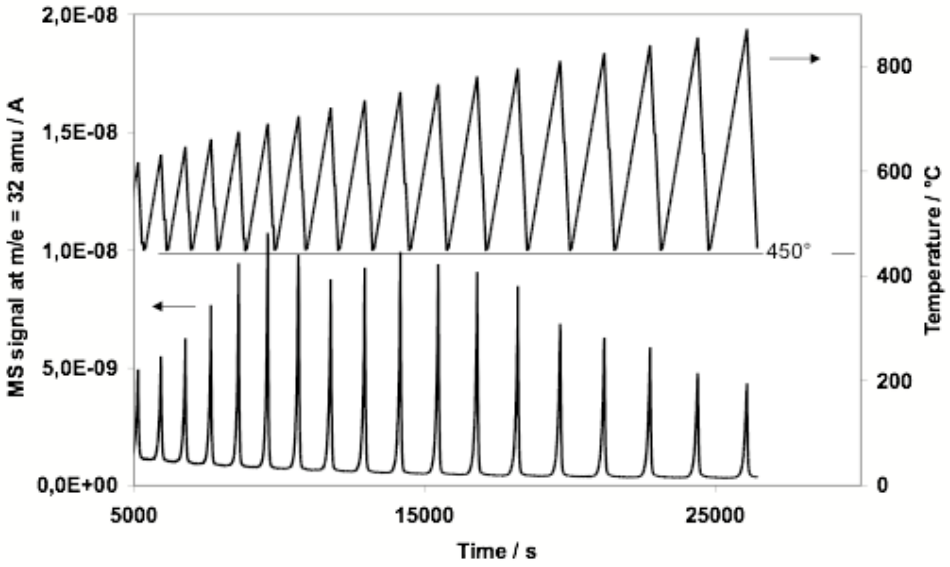

Figure 4.5: *Saw-tooth heating program and corresponding MS signal at m/e=32amu (ST50 sample).*

Fig. 4.7 shows the Arrehenius plot of oxygen partial TPDs for ST50 sample, calculated from the curves shown in Fig. 4.6. The complete TPD is also presented in the Arrhenius plot. Obviously, in the Arrhenius plot of ITPD data, one can observe four families of lines, characterised by their average slope, and corresponding to the four shoulders or peaks, α, β, γ, and δ. Using least squares fitting, a regression was applied to the linear part of the Arrhenius transform of each partial TPD in order to calculate the apparent energy E_{app}, which is directly proportional to the slope ($-E_{app}/R$) of each line. The values of E_{app} calculated by this way are plotted in Fig. 4.8 for ST30 and in Fig. 4.9 for ST50, with respect to the percentage of total oxygen desorbed below 850°C.

Four families of desorbed oxygen are evidenced, characterised by quite different average E_{app} values and corresponding to α, β, γ and δ shoulders or peaks . E_{app} values for ST30 are: 100±12 kJ·mol^{-1} (α), 180±10 kJ·mol^{-1} (β), 260±30 kJ·mol^{-1} (γ), and 330±3 kJ·mol^{-1} (δ) and for ST50: 115±15 kJ·mol^{-1} (α), 180±13 kJ·mol^{-1} (β), 265±19 kJ·mol^{-1} (γ), and

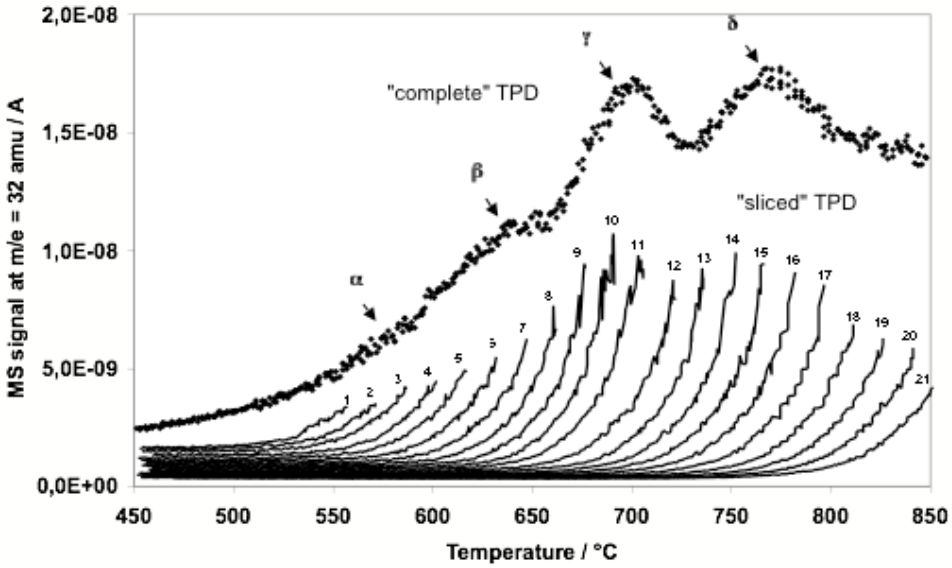

Figure 4.6: *Plots of complete TPD and sliced TPD (ITPD) profiles as a function of temperature (restricted to ascending parts) for ST50 sample.*

325±10 kJ·mol^{-1} (δ). For a given family, average E_{app} values are obviously very close for both samples. The main difference is the relative amount of each family. For ST30 sample, more weakly bonded species (corresponding to α, β, and γ) correspond to about 55% of the total desorbed dioxygen, while it is about 75% for ST50 sample. Therefore, the surface chemistry of ST50 sample seems to favour the more weakly bounded oxygen species. The literature data obtained with SnO_2 [36] are also plotted for comparison in Fig. 4.9 . E_{app} obtained values gather around plateaus at 285±10 kJ·mol^{-1} and 334±8 kJ·mol^{-1}, respectively, corresponding to the two peaks composing the whole TPD spectrum of SnO_2. These values are very close to those calculated for states γ and δ in both ST30 and ST50 samples. The main difference is, therefore, the presence of more weakly bonded species in ST30 and ST50 samples, corresponding to states α and β, which were not detected in SnO_2.

The apparent desorption frequency factor A_{app} can be calculated from the previous data set using Eq. 4.8. N and N_{tot} can be calculated by experimental data, as already explained in Par. 4.1. By considering the medium partial TPD for each family, the coverage θ of the

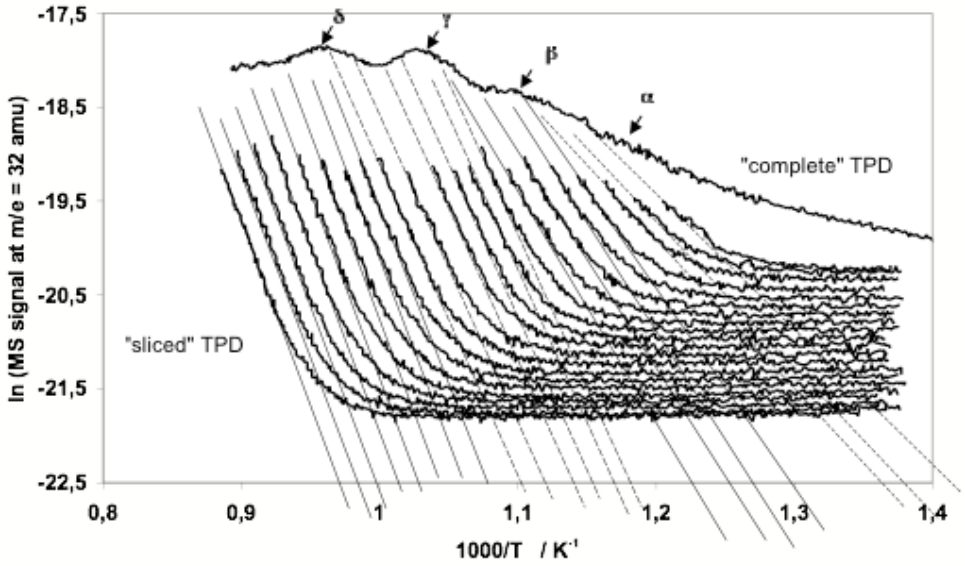

Figure 4.7: *Arrhenius transforms of partial TPDs (ITPD) for ST50 sample and linear fit of the linear part of each curve.*

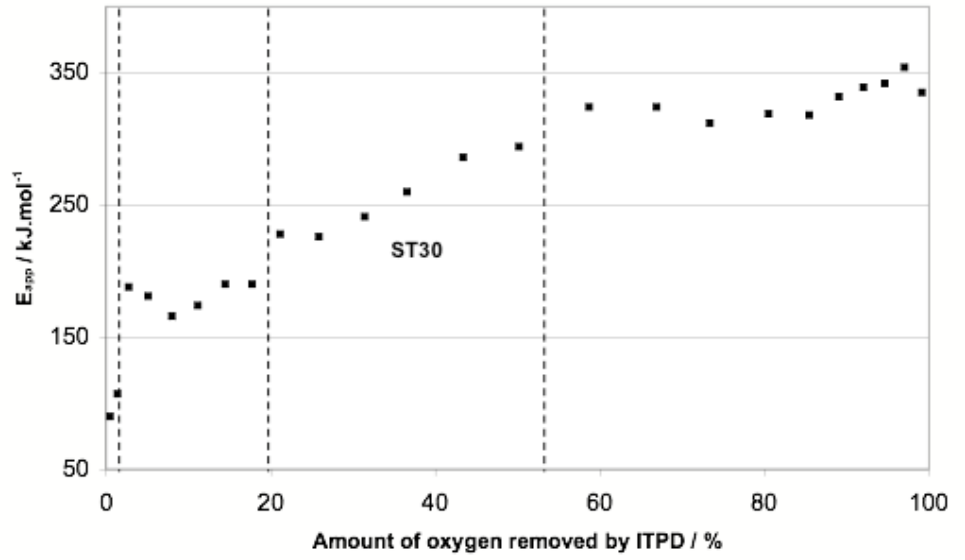

Figure 4.8: *Variation of E_{app} with respect to the amount of oxygen removed below 850°C for ST30 sample.*

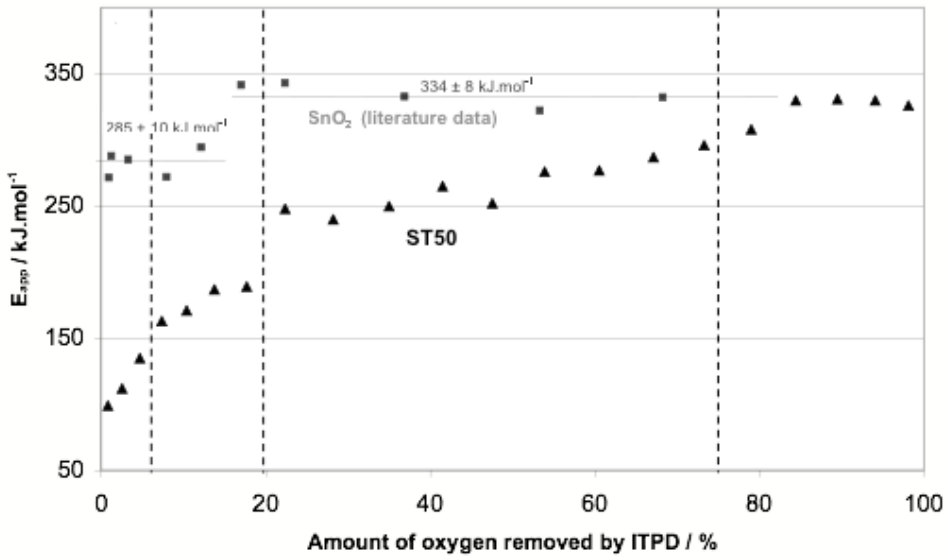

Figure 4.9: *Variation of E_{app} with respect to the amount of oxygen removed below 850°C for ST50 sample. Literature data obtained with SnO_2 are plotted for comparison [36].*

state concerned can be chosen close to 0.5 so that $f(\theta)$ is close to one. This procedure is sufficiently accurate to assess the order of magnitude of A_{app}. Calculated A_{app} values for ST30 and ST50 samples are reported in Tab. 4.3, with the corresponding E_{app} values and percentage of the total evolved oxygen.

Concerning the state δ, for both ST30 and ST50 samples, A_{app} calculated values are close to the frequency factor value of 10^{13} s^{-1}, provided by the classical Eyring's theory [39]. This observation strongly suggests that re-adsorption during ITPD runs may be ruled out for this state and that the apparent energies E_{app} are equal to activation energy of desorption E_{des}. Such high E_{des} values (more than 300 kJ·mol^{-1}) are generally assigned to surface or lattice O^{2-} species desorbing from metallic oxides [40, 41, 42]. Oviedo and Gillan [43] assigned the higher temperature states found by TPD to lattice oxygen from bridging and perhaps in-plane sites. For β and γ states, the calculated A_{app} values are about $2{\cdot}10^{11}$ and $1{\cdot}10^{8}$ s^{-1}, respectively. These values are several orders of magnitude lower than the 10^{13} s^{-1} value, strongly suggesting that re-adsorption does occur for this states during ITPD runs. In this case, apparent energies E_{app} are equal to heats of adsorption E=-

Table 4.3: Calculated A_{app} values for ST30 and ST50 samples with corresponding E_{app} values and percentage of the total evolved oxygen.

	$A_{app}(s^{-1})$		$E_{app}(kJmol^{-1})$		% des O_2	
Sample	ST30	ST50	ST30	ST50	ST30	ST50
State						
α	$4 \cdot 10^4$	$4 \cdot 10^4$	100 ± 12	115 ± 15	2	6
β	$6 \cdot 10^7$	$2 \cdot 10^8$	180 ± 10	180 ± 13	18	14
γ	$2 \cdot 10^{11}$	$2 \cdot 10^{11}$	260 ± 30	265 ± 19	33	56
δ	$5 \cdot 10^{12}$	$9 \cdot 10^{12}$	330 ± 3	325 ± 10	47	24

ΔH. Despite of many trials by several authors [37, 44, 45] such intermediate temperature state (β and γ) seems more difficult to assign: it may be O^- or O^{2-} species. Re-adsorption is also evident for α state, even if the very small amount of corresponding species (2-4 % of total desorbed O_2) does not allow a valuable determination of E_{app} and A_{app}.

This first TPD and ITPD study on Sn, Ti mixed oxides has demonstrated that oxygen species, both molecular and atomic, desorb from the surface of these materials employed as chemoresistive gas sensors and considered a stable alternative to the more used SnO_2 [35]. The presence of surface oxygen species has a considerable importance in the solid-gas interaction, since sensing mechanism is based on the role of adsorbed oxygen on the surface of the sensitive material, as explained in Par. 1.3. ITPD analysis, in particular, has shown the presence of four different shoulders or peaks (α, β, γ, δ) corresponding to four families of desorbed oxygen species. Except for the strong bonded species (states δ), readsorption occurs for the other states. This characteristic may represent an advantage for sensing mechanism, because further oxygen adsorptions enhance sensor reversibility and reactivity and, thus, response to gases. Morevover, the range of temperatures of desorption of weaker bonded states (about 450°C-700°C) rather matches with sensor operating temperatures (about 400°C-650°C) (see Ch. 5).

Chapter 5

Alkane sensing

Light alkanes are simple molecules characterised by short-single-bonded chains. These gases have been employed in many different fields since relatively recent years. The use of methane and propane for combustion is far-back recognised, while propane can also be employed to produce hydrogen by steam-reforming plants. The application of i-butane in gas-flow chambers for detection of charged particles in nuclear physics is well known. Detection of light alkanes may be of interest for different aspects. Therefore, many studies with the aim of creating a selective sensor system have been carried out in order to detect the presence and, ultimately, the leakages of these gases.

The recognition of chemoresistive metal oxides as materials for gas detection has been already remarked. Some results in alkane detection via chemoresistive materials have been published in [46, 47, 48, 49]. However, the mechanisms of surface reaction of these gases with the sensing materials are not deeply explained. This chapter describes the studies carried out with screen-printed films of metal oxides under different conditions as close to a real environment as possible.

5.1 Alkane oxidation via heterogeneous catalysis

The comprehension of the mechanism of interaction of the sensors vs. alkanes needs to introduce the concept of alkane oxidation via heterogeneous catalysis. The interpretation is based on catalytic studies [50, 51, 52], which thoroughly describe a general scheme about

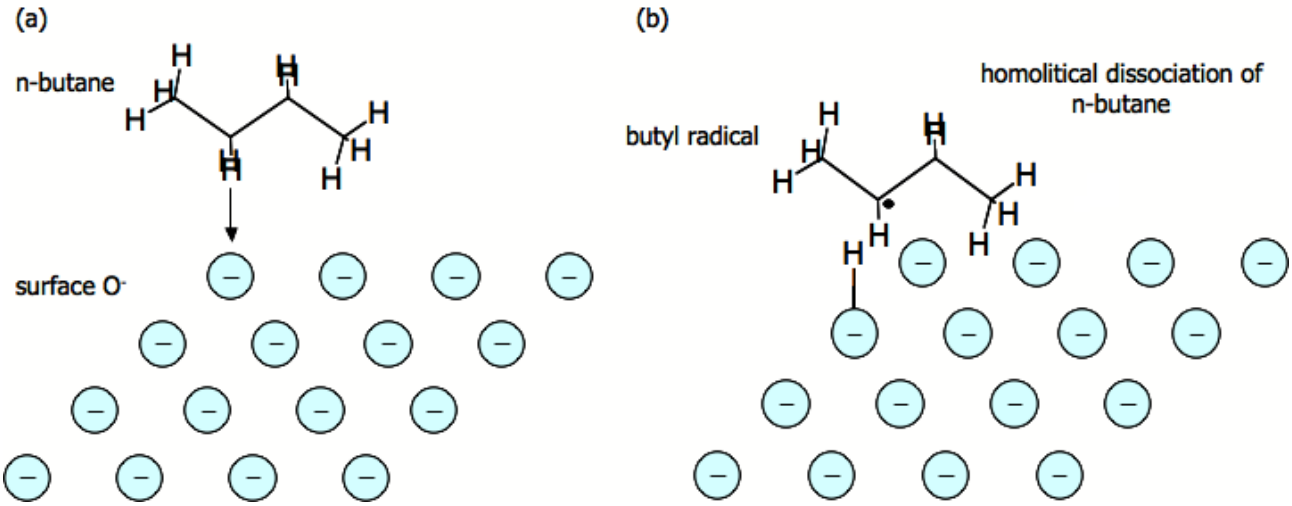

Figure 5.1: *First step of the reaction mechanism for n-butane at high and low temperatures: (a) C-H bond breaking and (b) butyl formation.*

reaction mechanisms between light alkanes and a catalytic surface, with particular emphasis to metal oxides. Alkane oxidation follows different routes, depending on the reaction temperature and the catalytic material. Very high- (over 1000°C) and low-temperature (400-700°C) mechanisms depend on the materials and on the gases. In any case, the initial step of the reaction consists of C-H homolytic bond breaking, which is considered as the rate-limiting step, then a hydrogen atom is being adsorbed onto the surface. Fig. 5.1 shows *n*-butane behaviour as an example. At very high temperatures (Fig. 5.2) the alkyl radical, which has been formed, as a result of the C-H bond breaking, is being released in the gaseous phase. Here homogenous gas-phase reactions proceed rapidly because of the high reactivity of the radical. At lower temperatures (Fig. 5.3) the alkyl radical formed is adsorbed on the surface and, as a consequence of a second C-H bond breaking (this time is a β-elimination), an alkene is formed. Readsorption of the alkene may occur: this will cause further reactions that yield degradation products. The adsorbed alkyl may undergo another mechanism, involving formation of a surface alkoxide intermediate, which could be further oxidized to aldehyde and carboxylates and eventually to carbon oxides.

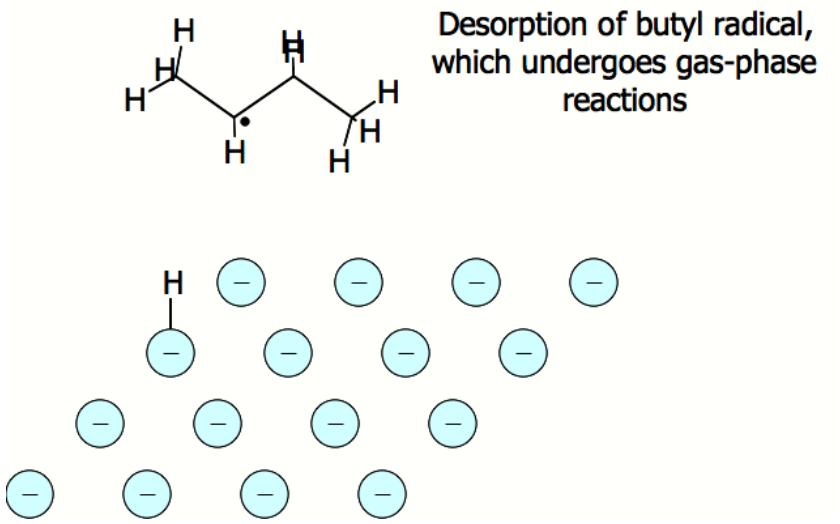

Figure 5.2: *Second step of the reaction mechanism for n-butane at high temperatures.*

5.2 Conduction measurements

Dedicated experiments were performed with a set of films of SnO_2, TiO_2 and solid solutions of Sn and Ti mixed oxides. Responses to light alkanes under dry and wet conditions and in presence of ethanol, as interfering gas, are shown in this section. Different behaviours depending on the operative temperature were highlighted. Comparisons among results obtained under the three different conditions were provided.

5.2.1 Experimental conditions

The metal oxides used for the experiments are SnO_2, TiO_2, ST10, ST30, ST50, ST70, ST90 and STN. Nanostructured powders were produced following the methods described in Par. 3.1. A ChemBET3000 Quantachrome instrument (see App. A) was employed in order to measure the specific surface areas of ST powders by the BET technique (see Tab. 5.1 for the calculated values). Sensing films (see Par. 3.2 for further details) were screen-printed

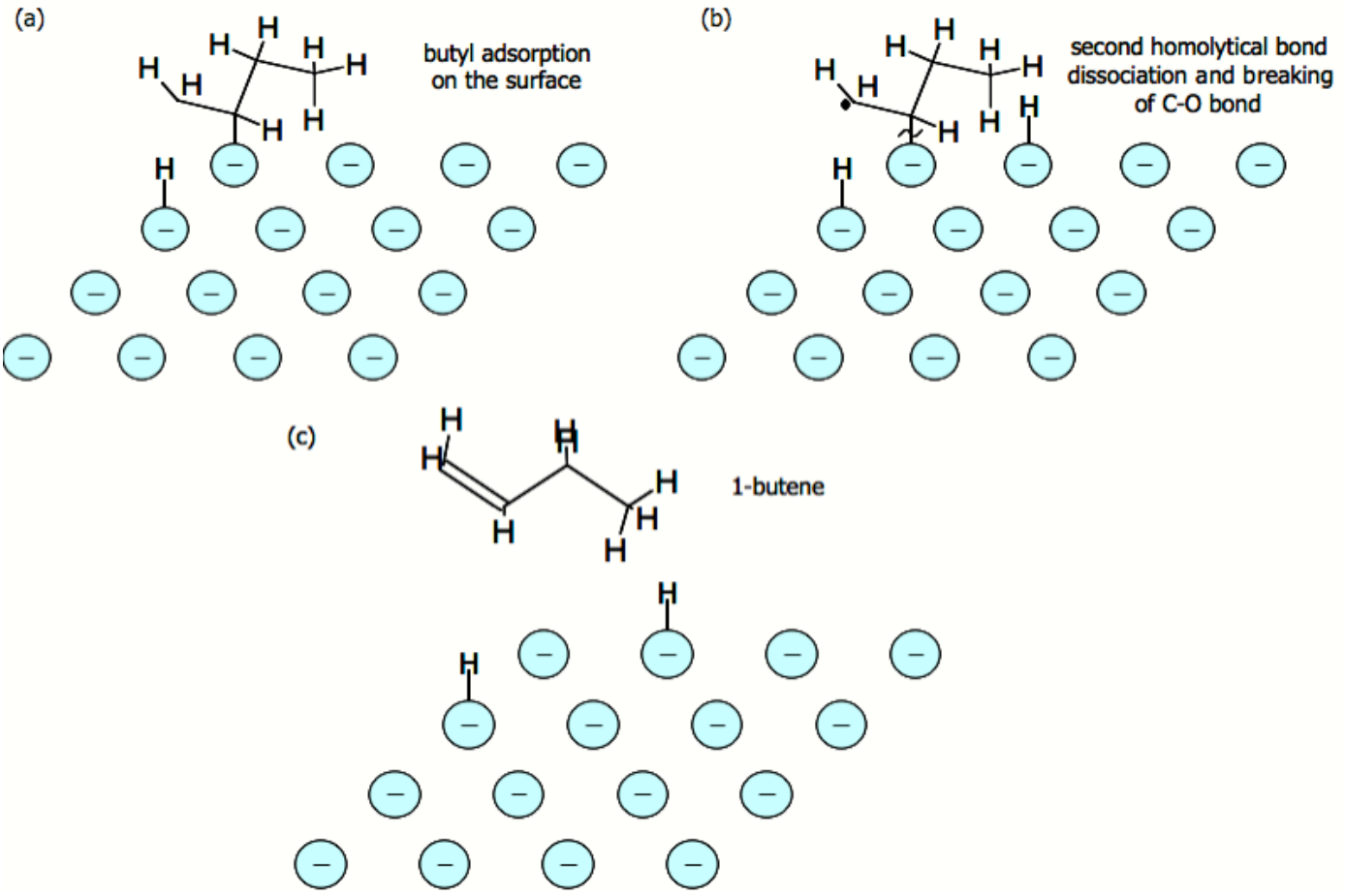

Figure 5.3: *Second step of the reaction mechanism for n-butane at low temperatures: (a) adsorption of butyl radical on the surface of the catalytic site and formation of C-O bond, (b) second C-H bond breaking and C-O breaking and (c) formation of butene.*

onto miniaturized laser precut alumina equipped with a heater on the backside, a Pt-100 resistor controlling sensor operating temperature and a golden front interdigitated contact. Successively, firing was performed for 1 h at 650°C under air flow condition. The thickness of the films was 20-30μm [53].

Table 5.1: Specific Surface Area values. (ST50 was not measured).

$STpowders$	$SpecificSurfaceArea(m^2/g)$
$ST10$	43.6 ± 0.05
$ST30$	71.8 ± 0.05
$ST70$	62.6 ± 0.05
$ST90$	37.4 ± 0.05

Film conductance was measured by the gas-flow technique in a sealed test chamber. The sensor is inserted in an electric circuit, equipped with an inverting operational amplifier, thus its transfer function is:

$$V_S = -\frac{R_C}{R_S} V_B \tag{5.1}$$

where V_B is the bias tension (set at -5 V), R_C the feedback resistance and R_S is the resistance of the sensor. Voltage V_S is measured through the four point method. Thus, the expression for the conductance, G, holds:

$$G = \frac{1}{R_S} = -\frac{V_S}{V_B R_C} \tag{5.2}$$

Finally, the response of the sensor is the ratio of the film conductance in gas and that in air (G_{gas}/G_{air}).

Relative humidity (RH) of the gas flow was monitored through a HIH-3610-Series Honeywell humidity sensor. Dry (RH<5% at 25°C) and wet (40%<RH<50% at 25°C) carriers were chosen to investigate the interference of water and, in turn, its effects on the gas response. Alkanes and ethanol were supplied by certified bottles and fed into the test

chamber at 500 cm^3/min total flow. In particular, the following concentrations were chose: 100 ppm of C2-C4 alkanes and 500 ppm of methane, because such values are by far lower than the alarm levels (Tab. 5.2); 10 ppm of ethanol, because higher concentrations are prevented by the use of a filtre (NORIT RB1 activated carbons), installed upstream the test chamber. Thus, the size of the filtre and the total flow were set in order to obtain an estimated maximum of 5 ppm of ethanol to be fed into the test chamber, when 5000 ppm were supplied. Electrical measurements were performed at several operating temperatures within 300 and 650°C.The filtre was tested vs. 2500 ppm or 1670 ppm of methane and 5000 ppm of ethanol.

Table 5.2: Lower and upper explosive limits for each alkane.

$Alkane$	$LEL(ppm)$	$UEL(ppm)$	$Density(air = 1)$
CH_4	50000	150000	0.60
C_2H_6	31000	124500	1.00
C_3H_8	21000	101000	1.60
C_4H_{10}	18600	84100	2.10

5.2.2 Results and discussion

Dry and wet conditions

First, the response, G_{gas} /G_{air}, of the sensors vs. alkanes was investigated under dry condition. The response was found to increase with the number of molecular carbon atoms (C1-C4) within the temperature range investigated (450-650°C, see Figs. 5.4-5.6). The sensors best performed at 550°C and the difference in response due to the number of molecular carbon atoms (C1-C4) became still more apparent. The ST films responded according to the decreasing trend: ST50, ST30, ST70, ST10, ST90; the STN turned out to be the most performing film at each operational temperature and for each gas.

The increasing response as a function of the number of carbon atoms can be justified by considering that the rate-limiting step of the reaction mechanism is the first C-H bond

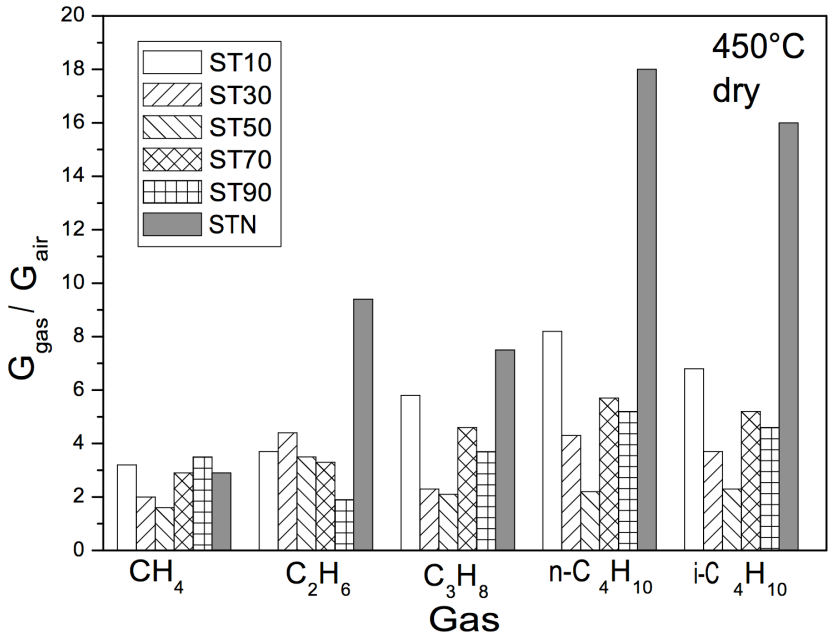

Figure 5.4: *Responses to 500 ppm of CH_4 and 100 ppm of C2-C4 alkanes at 450°C under dry condition.*

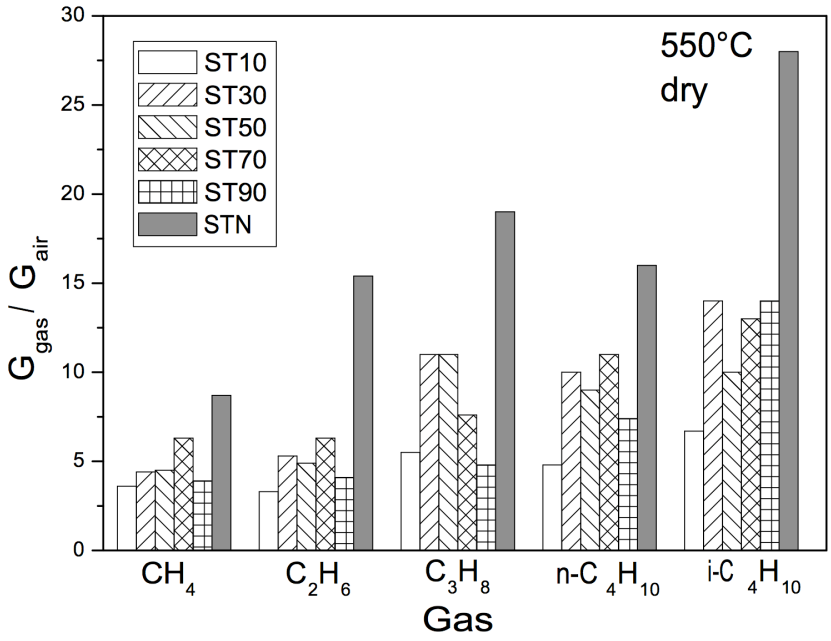

Figure 5.5: *Responses to 500 ppm of CH_4 and 100 ppm of C2-C4 alkanes at 550°C under dry condition.*

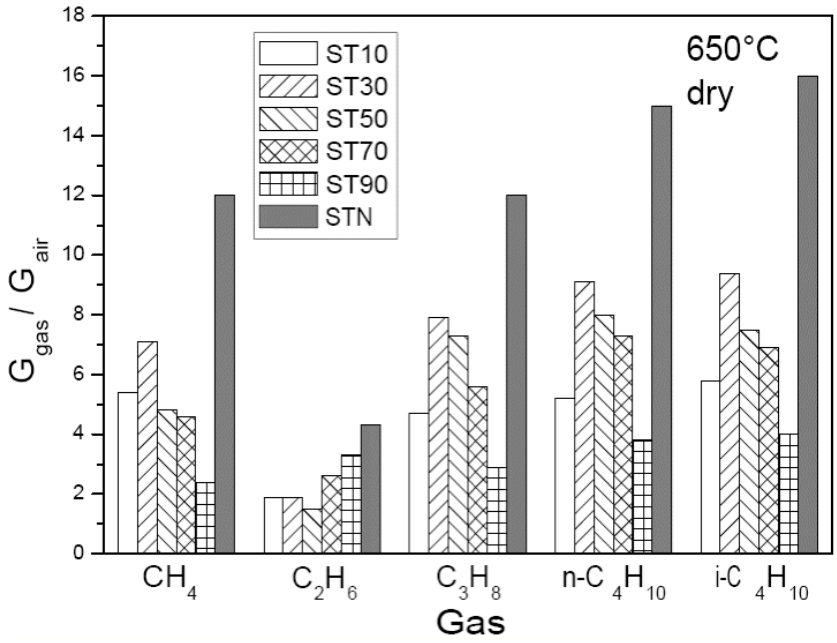

Figure 5.6: *Responses to 500 ppm of CH_4 and 100 ppm of C2-C4 alkanes at 650°C under dry condition.*

breaking, which is more probable in a long hydrocarbon chain (that is to say with more than three carbon atoms in our case). To support this assumption, Tab. 5.3 contains homolytic bond dissociation energies for each alkane. As one can see, the dissociation at the tertiary carbon atom demands a lower energy. Indeed, *i*-butane, which is the only alkane with such a carbon atom, is the most detectable gas, sequentially followed by *n*-butane (containing two secondary carbon atoms) and then propane (containing only one secondary carbon atom). On the other hand, methane, which has just one carbon atom, is characterised by a higher dissociation energy, thus a lower response.

The films were investigated under wet condition (Figs. 5.7-5.9) at temperatures within 450 and 650°C. The most evident observation is a significant decrease in response with respect to the dry case under the same condition. At 650°C the response fell off by about three times with respect to the dry case. In contrast with the dry case, the response of the films enhanced with increasing temperature till 650°C, i.e. the highest temperature investigated. As for under dry condition, STN turned out to be the most performing film, and all the films were more sensitive to heavier alkanes.

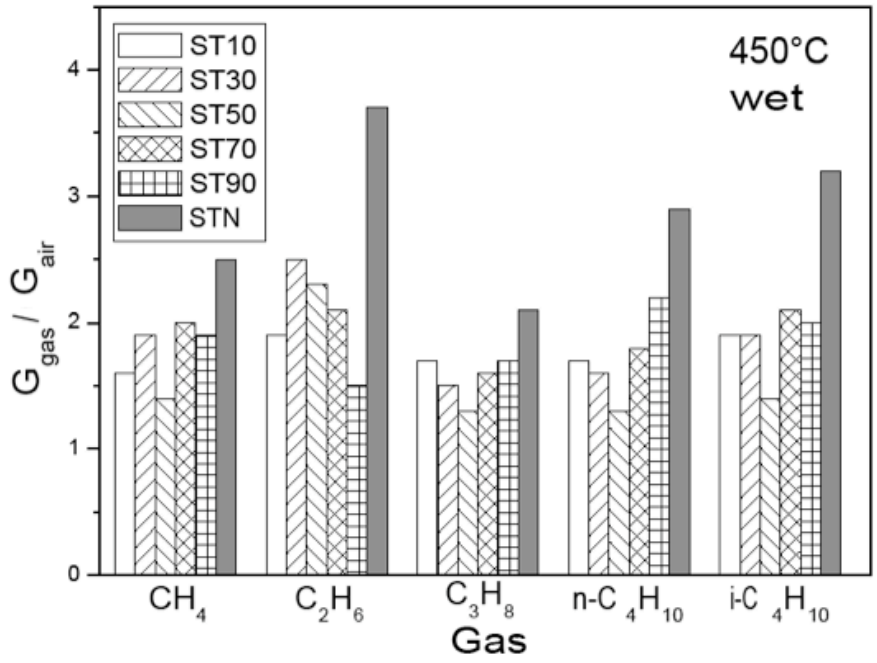

Figure 5.7: *Responses to 500 ppm of CH_4 and 100 ppm of C2-C4 alkanes at 450°C under wet condition.*

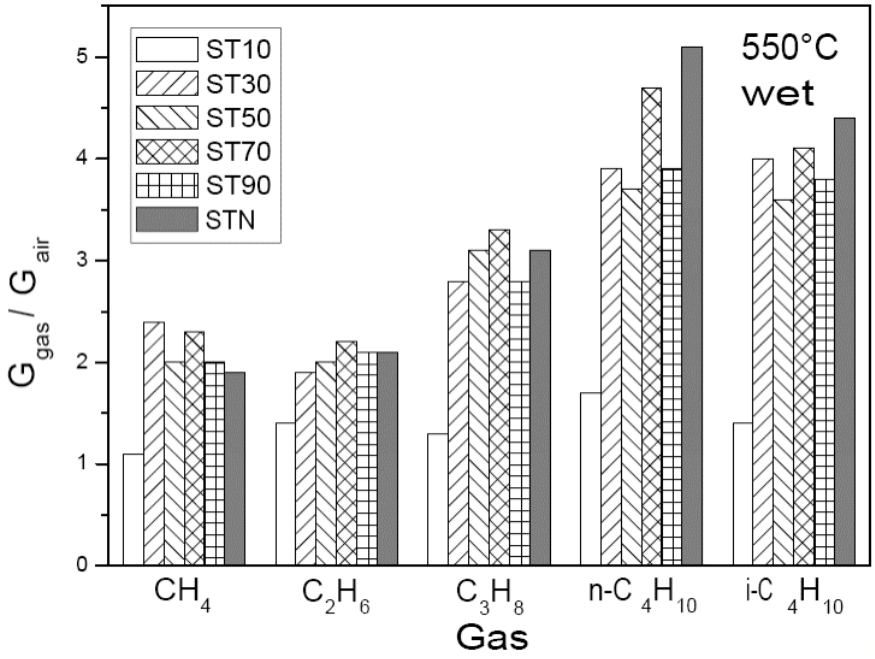

Figure 5.8: *Responses to 500 ppm of CH_4 and 100 ppm of C2-C4 alkanes at 550°C under wet condition.*

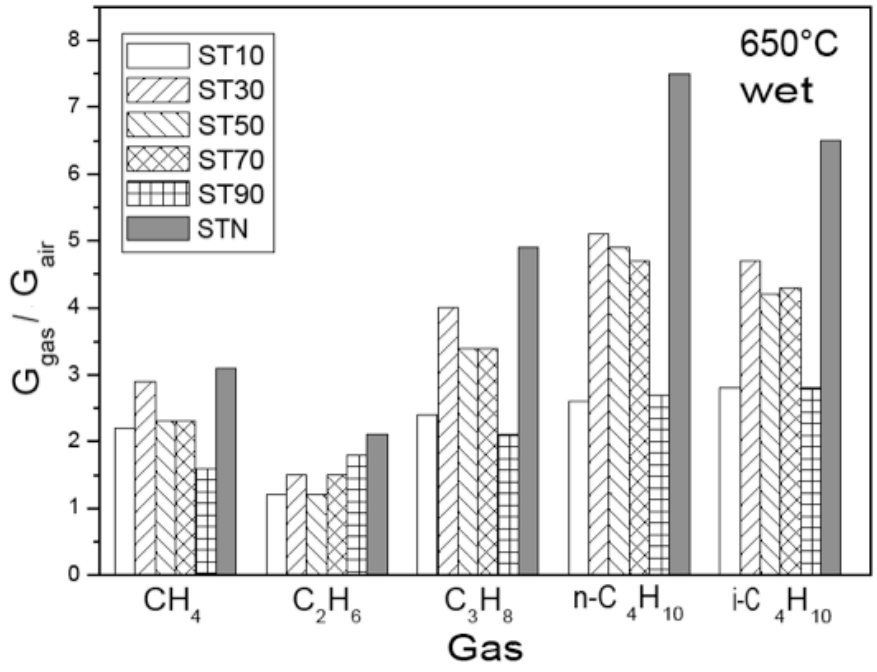

Figure 5.9: *Responses to 500 ppm of CH_4 and 100 ppm of C2-C4 alkanes at 650°C under wet condition.*

Table 5.3: Homolytic bond dissociation energies, ΔH^{Θ}, at 25°C.

Alkane	$\Delta H^{\Theta}(kcal/mol)$
$C_3 - H$	104
$C_2H_5 - H$	98
$n - C_3H_7 - H$	98
$i - C_3H_7 - H$	95
$i - C_4H_9 - H$	92

The significant decrease in response under wet condition can be interpreted as an effect of OH^- adsorption on the surface of the film, which competes with the reaction of alkanes. As depicted in Fig. 5.10, the effect of water molecules interacting with the surface consists in releasing H atoms and in creating an OH^- group on the surface. Thereby, the number of active sites on the surface available for reaction with alkanes decreases. However, as temperature increases, adsorbed OH^- ions leave the reactive sites and thus water molecules interfere less with the alkane reaction. Information about water desorption from SnO_2 and TiO_2 surfaces were retrieved from literature [54, 55] to support such hypothesis. In the case of SnO_2, it is reported that OH^- groups leave the surface at about 400°C, while recombination of dissociated water is seen with a desorption peak above 670°C for TiO_2. These temperatures for water desorption are consistent with the experimentally observed film responses.

Ethanol interference

First, the behaviour of two films, SnO_2 and STN, was investigated in the presence of an active carbon filtre at an intermediate temperature (550°C) under wet condition [56]. The insertion of the filtre makes the relative humidity RH decrease from about 45% down to about 25% at 25°C. The response of the films vs. 2500 ppm of methane with and without the filtre is shown in Fig. 5.11. The response was found to be higher with the filtre and the STN film turned out to be the best performing sensor. According to the specifications of the manufacturer of the filtre, absorption of methane by the filtre is negligible. The response increases with the filtre on, because it reduces the interference of water in the reaction between methane and the film (this behaviour was described in the previous section, [57]).

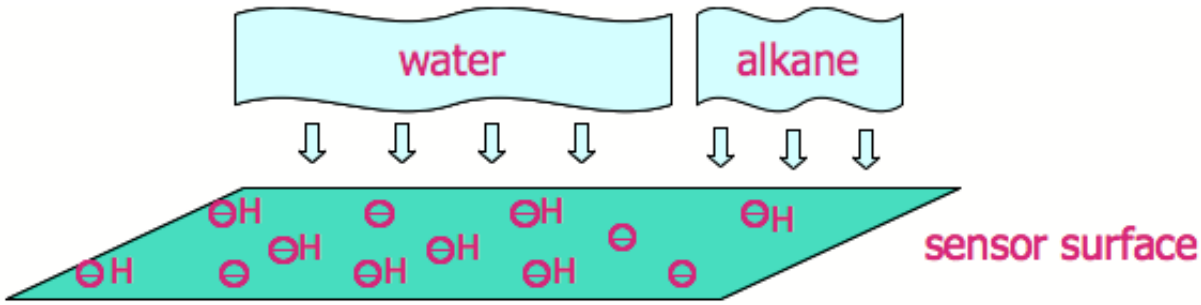

Figure 5.10: *Competion between water and alkane under wet condition: a smaller number of available sites is evident.*

Fig. 5.12 shows the responses vs. 5000 ppm of ethanol and 1670 ppm of methane with the filtre on, separately (a) and simultaneously (b). In the latter, normalisation is made relative to the conductance achieved at a 5000 ppm of ethanol (with filtre on).

After testing the filtre, a set of systematic measurements of the conductance of the sensors was carried out. Since a maximum concentration of 5 ppm of ethanol can be released by the filtre, all the electrical measurements were performed with 10 ppm of ethanol and under wet condition, in order to overestimate any possible interfering condition and to take account of the active carbon aging.

Ethanol was measured at temperatures within 300°C and 650°C, in order to estimate the extent of the response. The signal of ethanol (see Fig. 5.13) initially increases with temperature, then starts decreasing at higher temperatures. Fig. 5.13 shows that the response peaks at 400°C for the SnO_2 layer and at 550°C for the TiO_2. The other layers peak at intermediate temperatures. The behaviour of ethanol is due to its favoured interaction with the sensor surface in comparison to that of the alkanes, as it occurs with water [57]. The oxidation of ethanol takes place on the surface of the sensor via the dehydrogenation to acetaldehyde, involving the adsorbed oxygens and the OH^- group [58]:

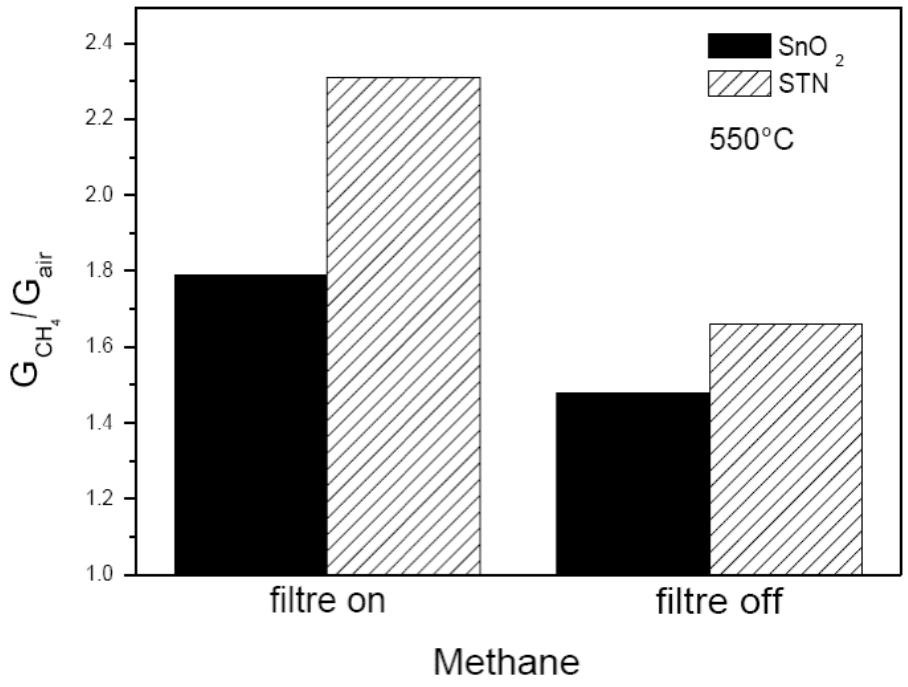

Figure 5.11: *Responses to 2500 ppm of CH_4 with and without filtre at 550° C under wet condition.*

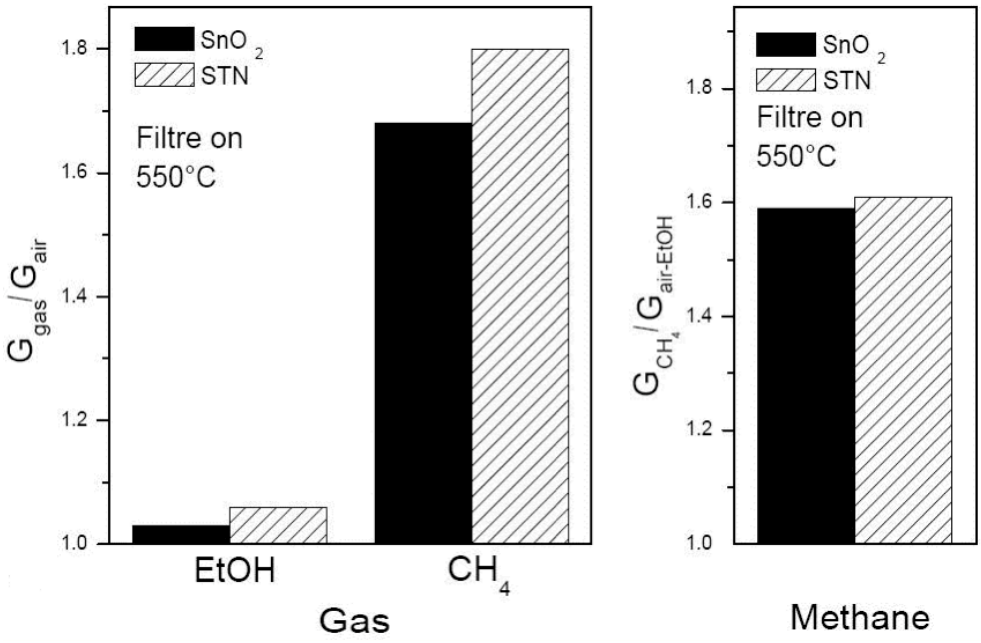

Figure 5.12: *Responses to 1670 ppm of CH_4 and 5000 ppm of C_2H_6O with filtre at 550¡C under wet condition (a); responses to 1670 ppm of CH_4 in presence of 5000 ppm of C_2H_6O (b).*

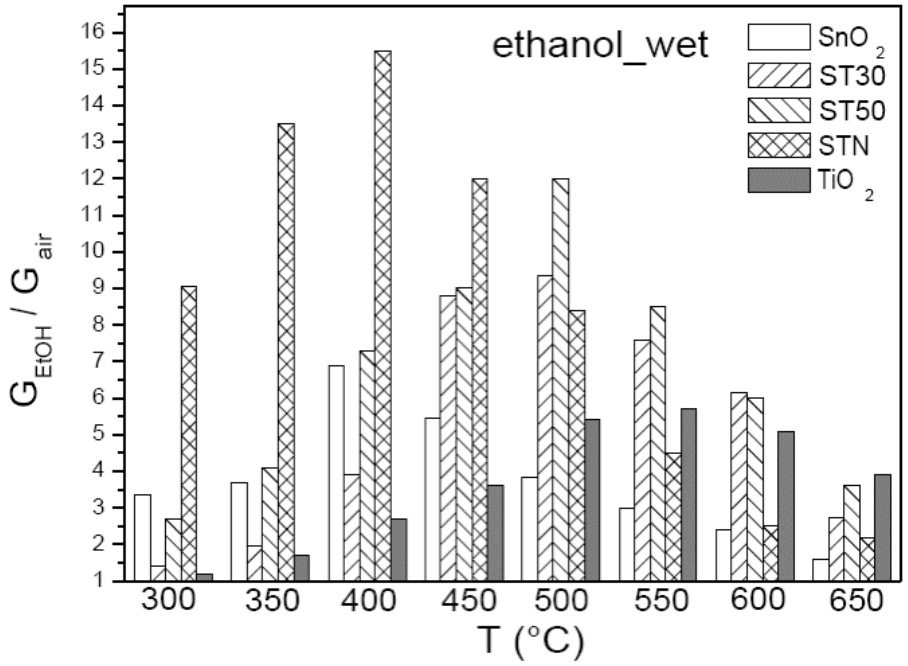

Figure 5.13: *Responses to 10ppm of C_2H_6O at temperatures within 300°C and 650°C under wet condition.*

$$O_{ads} + C_2H_5OH \rightleftharpoons CH_3CHO + H_2O \tag{5.3}$$

The electrical measurements achieved for alkanes were firstly considered, then the measurements for alkanes in presence of ethanol. On the basis of the previous results (5.2.2, [57]) and previous studies [59, 60], the response vs. light alkanes is significantly high, when operating above 450°C. Figs. 5.15-5.16 show the responses vs. alkanes compared with that achieved for ethanol at temperature within 450°C and 650°C under wet condition. The STx and STN films turned out to be the best performing sensors, while TiO_2 was too resistive to appreciate the variations induced by gases. Once again, the response of the sensors vs. alkanes increases with the number of carbon atoms, and with temperature, as a general trend [57, 59]. This behaviour has already been explained previously (see Par. 5.1 and Par. 5.2.2).

Finally, the interfence of ethanol was investigated by measuring the response of the sensors vs. alkanes under wet condition within 450°C and 650°C. On the basis of the

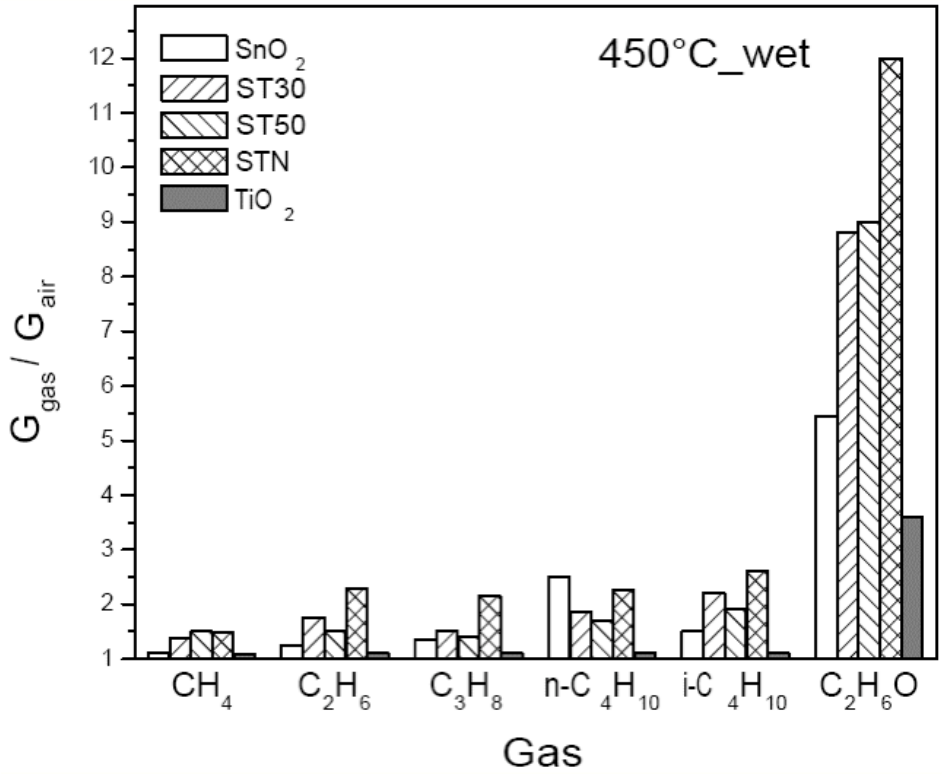

Figure 5.14: *Response to 500 ppm of methane, 100 ppm of C2-C4 alkanes and 10 ppm of* C_2H_6O *at 450°C underwet conditions.*

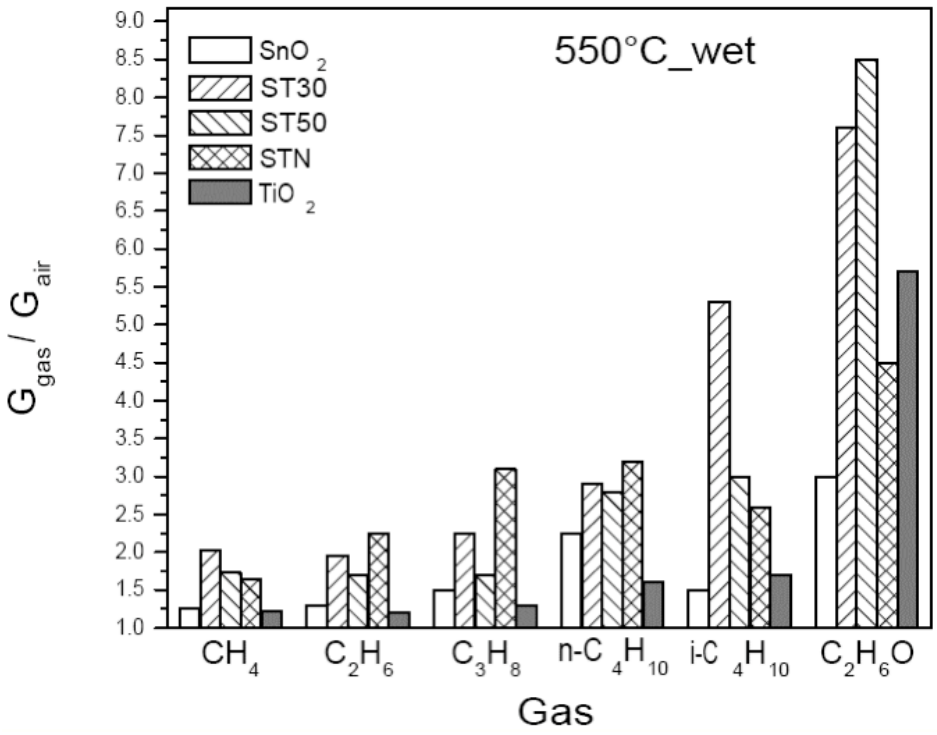

Figure 5.15: *Response to 500 ppm of methane, 100 ppm of C2-C4 alkanes and 10 ppm of* C_2H_6O *at 550°C underwet conditions.*

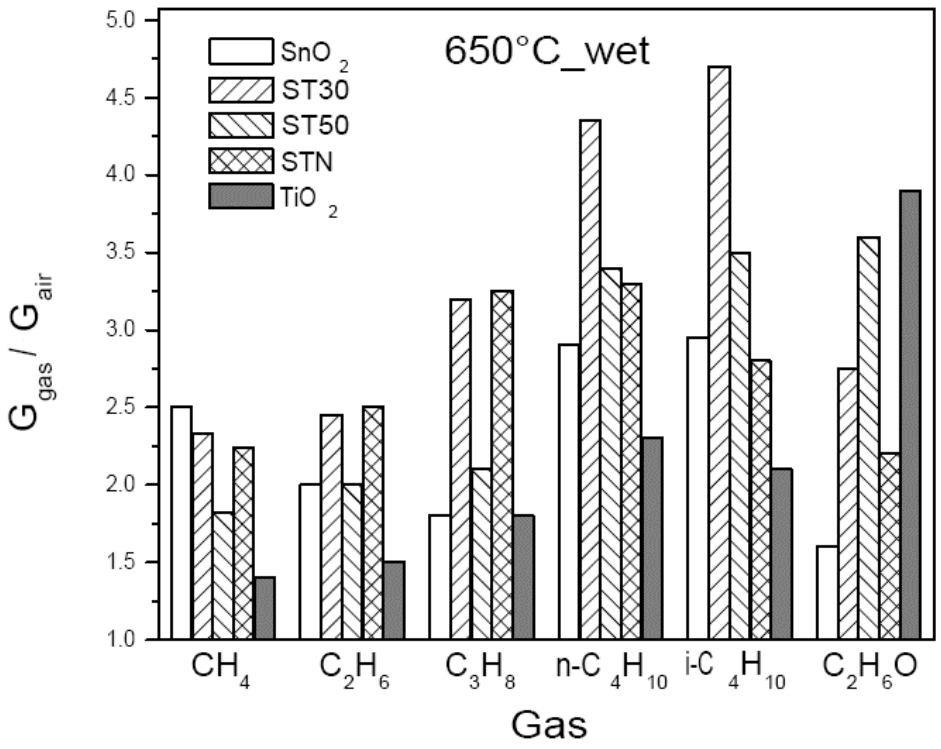

Figure 5.16: *Response to 500 ppm of methane, 100 ppm of C2-C4 alkanes and 10 ppm of C_2H_6O at 650°C underwet conditions.*

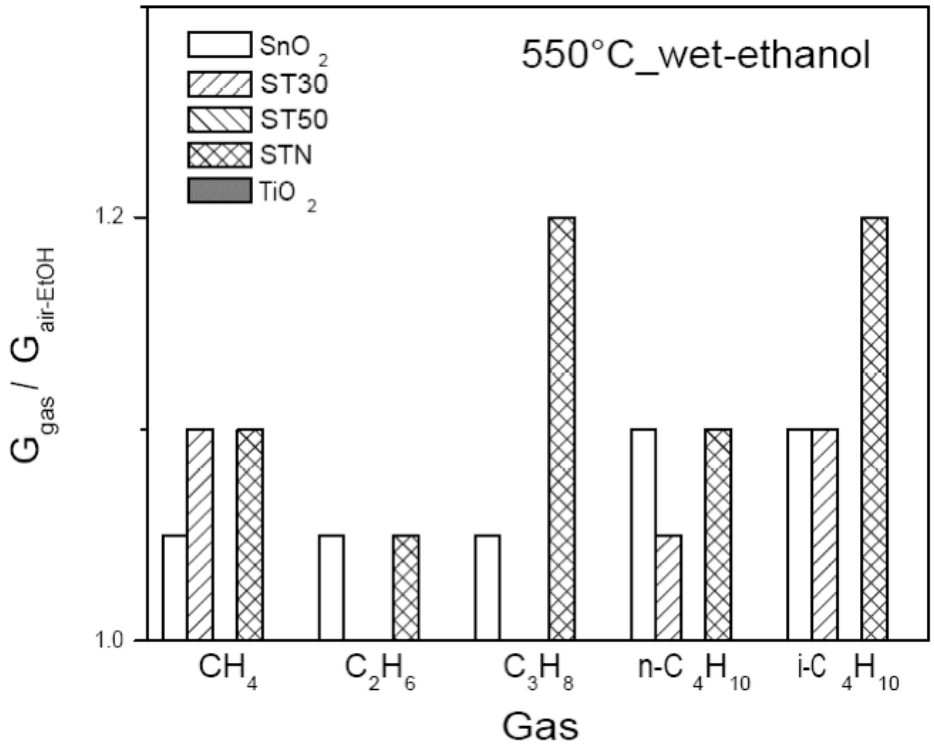

Figure 5.17: *Response to 500 ppm of methane, 100 ppm of C2-C4 alkanes in presence of 10 ppm of C_2H_6O at 550°C in wet conditions.*

previous observations, one expects that the SnO_2 layer sensitively responds to alkanes in presence of ethanol at 650°C, while the TiO_2 layer should be insensitive and the other layers should respond similarly to the SnO_2 film. Indeed, a negligible response below 550°C and a significant sensing performance within 550 and 650°C were observed for all the sensors (see Figs. 5.17 and 5.18). Ethanol lowered the response to alkanes, even if the sensors still sensitively detected such gases at high temperatures. STN and SnO_2 turned out to be the best performing films, especially at 650°C.

All the electrical measurements are characterised by sensor response and recovery times of about 10 and 20 min, respectively.

The present study demostrates that it is possible to sensitively detect alkanes in presence of a maximum concentration of 10 ppm of ethanol under wet condition. In particular, the STN and the SnO_2 films are suitable for this purpose at 650°C. If the concentration

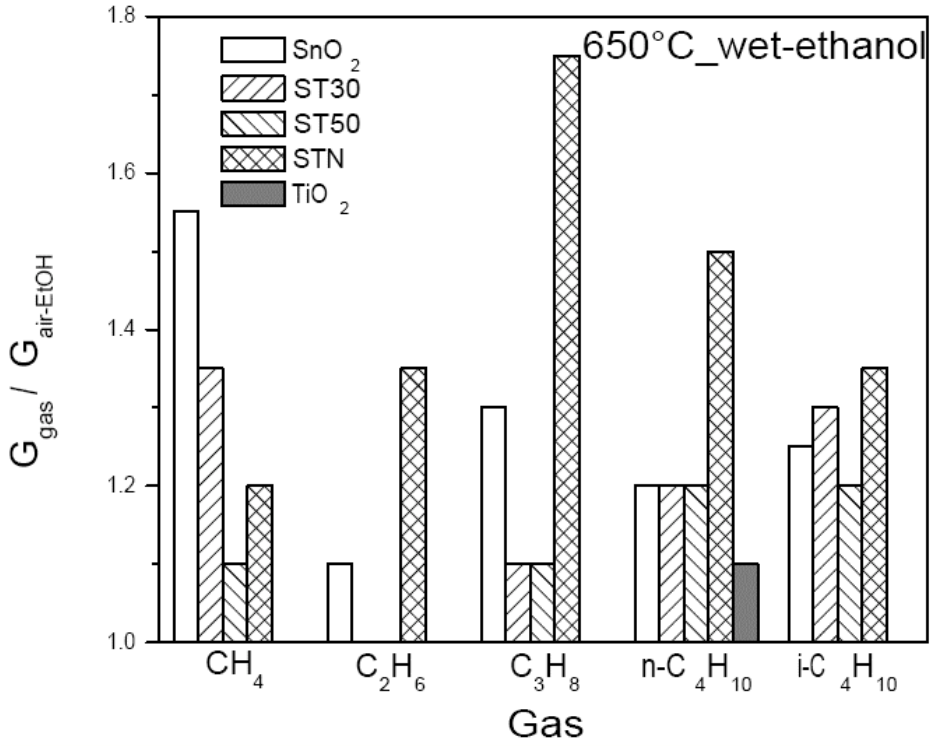

Figure 5.18: *Response to 500 ppm of methane, 100 ppm of C2-C4 alkanes in presence of 10 ppm of C_2H_6O at 650°C in wet conditions.*

of ethanol were constant, it would be possible to determine the concentration of alkanes through the knowledge of the calibration curve. However, unexpected changes in the environment or worsening of the filtre condition would change the concentration of ethanol. In this case, an additional sensor capable of detecting specifically the concetration of ethanol is needed. This device could either be the STN or the SnO_2 layer operating at maximum 400°C. In fact, at this temperature, the films proved to be insensitive to alkanes. When two interfering gases are present, a two-dimension-calibration surface is needed. This surface is determined through the interpolation of several experimental calibration curves of one gas. Each curve is built, fixing the concentration of the second gas, according to the method in [61]. In this case, the knowledge of the calibration curve of the film sensitive to only ethanol and the calibration surface of the film sensitive to alkanes and ethanol will lead to the concentration of the alkane under consideration.

Conclusions

In this dissertation surface and conduction properties of metal-oxide semiconductors were studied, giving particular attention to the interaction mechanisms between those materials and gases.

Temperature programmed desorption techniques were chosen to investigate thermodynamic properties of nanostructured powders. O_2 desorption experiments provided promising results concerning the sensitivity of samples. SnO_2 was characterised by the highest amount of desorbed oxygen, while TiO_2 was the less performing powder. The amounts of oxygen species desorbed from samples STx were lower than those desorbed from SnO_2, but did not correspond to a mere linear combination of (1-x)SnO_2/xTiO_2, suggesting the formation of a mixed oxide with different properties from both SnO_2 and TiO_2. The desorbed amounts represented less than 10% of a compact monolayer of ions O_2^-, excluding bulk desorption. Four families of surface species were observed and corresponding energetic values were calculated. Except for the strong bonded species, readsorption occurred for the other states, representing an advantage for sensing mechanism, because further oxygen adsorptions enhance sensor reversibility and reactivity.

Thick film sensors were, then, tested for light alkane sensing. Conduction measurements were performed and resulted in positive responses under dry and wet conditions and in presence of ethanol, as interfering gas. The interaction mechanism of sensors vs. alkanes was interpreted on the basis of catalytic studied. The interference of water and ethanol was explained and the use of an active carbon filtre was proposed as a tool to hinder their negative effects on sensor response. The employed sensitive layers sensitively detected alkanes, even under wet condition and in presence of a maximum concentration of 10 ppm of ethanol. SnO_2 and STN-based films turned out to be suitable for this purpose at 650°C. Concrete indications about the building of a reliable and efficient device were suggested.

Appendix A

BET measurements

BET (Brauner, Emmet and Teller) theory, described in Par. 2.2.2, is the basis for analysis techniques for the measurements of the specific surface area of solids. Such parameter expresses the relationship between the total surface of the solid and the weight of the same one and usually is expressed in m^2/g.

This method uses the principle of the physical inert gas (usually, nitrogen) adsorption to vary the relationship between the partial pressure of nitrogen and its vapour pressure. It can be carried out under static or dynamic conditions. The first, under vacuum, comprises volumetric and gravimetric methods. The volumteric method consists in the introduction of a known volume of gas and employs the change of volumes of gas to calculate the adsorbed quantity; while gravimetric method is performed by means of a microbalance and its main adavantage is that the volume of the adsorption system is without importance [62, 63]. Under dynamic condition, on the other hand, vacuum is replaced with an inert gas stream.

A.1 Determination of the specific surface area

Recalling and rearranging Eq. 2.10, another form of BET equation is obtained [20]:

$$\frac{1}{W[(p_0/p)-1]} = \frac{1}{W_{mon}c} + \frac{c-1}{W_{mon}c}(p/p_0) \tag{A.1}$$

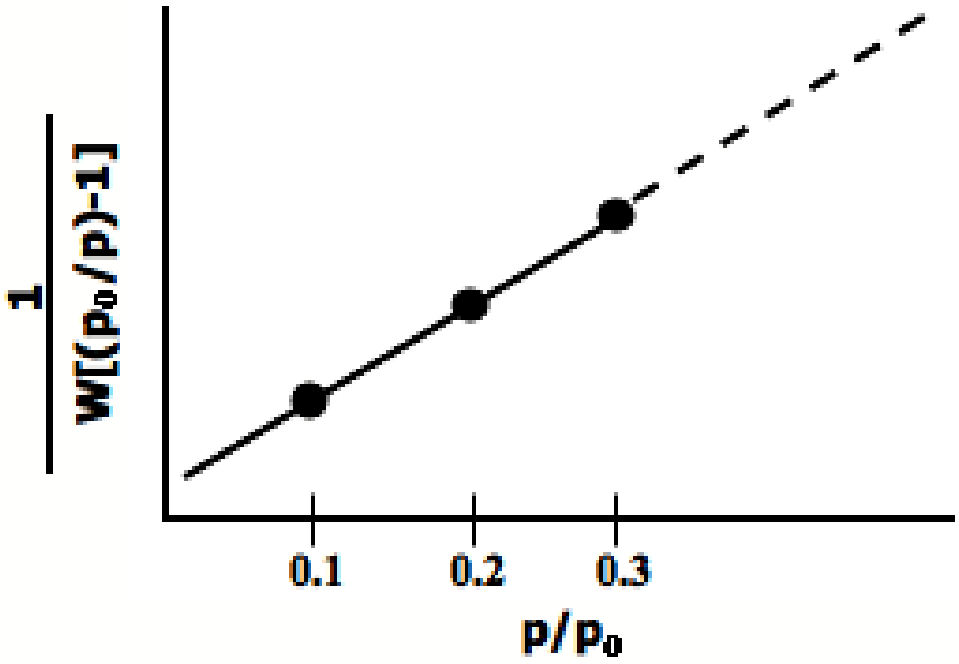

Figure A.1: *Linearisation of BET equation.*

W_{mon} is the weight adsorbed in a monolayer.

Linearisation of Eq. A.1, which consists in putting on a graph the left term, $\frac{1}{W[(p_0/p)-1]}$ versus p/p_0, gives a straight line usually in the range $0.05 \leqslant p/p_0 \leqslant 0.35$ (shown in Fig. A.1) [20, 64].

W_{mon} can be calculated from the intercept, $i=1/(W_{mon}c)$, and the slope, $s=(c-1)/(W_{mon}c)$:

$$W_{mon} = \frac{1}{s+1} \tag{A.2}$$

The total surface of the solid sample can be derived by the following expression:

$$S_t = \frac{W_{mon} N A_{cs}}{M} \tag{A.3}$$

N is the number of Avogadro ($6.023 \cdot 10^{23}$ molecule/mol), A_{cs}=16.2 $\AA^2$ (for nitrogen at 77 K) is the area covered by one molecule of gas adsorbed on a particle of the solid, M is the adsorbate molecular weight. BET equation needs at least three experimental points, determined at three different relative pressures (*multi-point method*).

Eq. A.1 can be simplified in order to calculate W_{mon} with a single experimental point (*single-point method*):

$$W_{mon} = W(1 - \frac{p}{p_0}) \tag{A.4}$$

In this case, the slope s=$1/W_{mon}$ and the total surface is determined through:

$$S_t = W_{mon}(1 - p/p_0)\frac{N}{M}A_{cs} \tag{A.5}$$

A relative pressure, p/p_0, of 0.3 gives a good general agreement with the multi-point method. The single-point method offers the advantage of simplicity and speed often with little loss in accuracy [20].

In the end, the specific surface area can be determined from the results of BET measurements:

$$A_{ss} = \frac{S_t}{W} \tag{A.6}$$

where W is the weight of the powder sample.

A.2 Experimental determination of the specific surface area

BET measurements were performed both in Ferrara and in Lyon. Sensor and Semiconductor Laboratory of Ferrara is equipped with a dynamic instrument, a Quantachrome Instruments ChemBET 3000 (see Fig. A.2), while IRCELYON with a Micromeritics TRISTAR 3000 (see Fig. A.3), which operates under volumetric condition.

Figure A.2: *A picture of ChemBET 3000.*

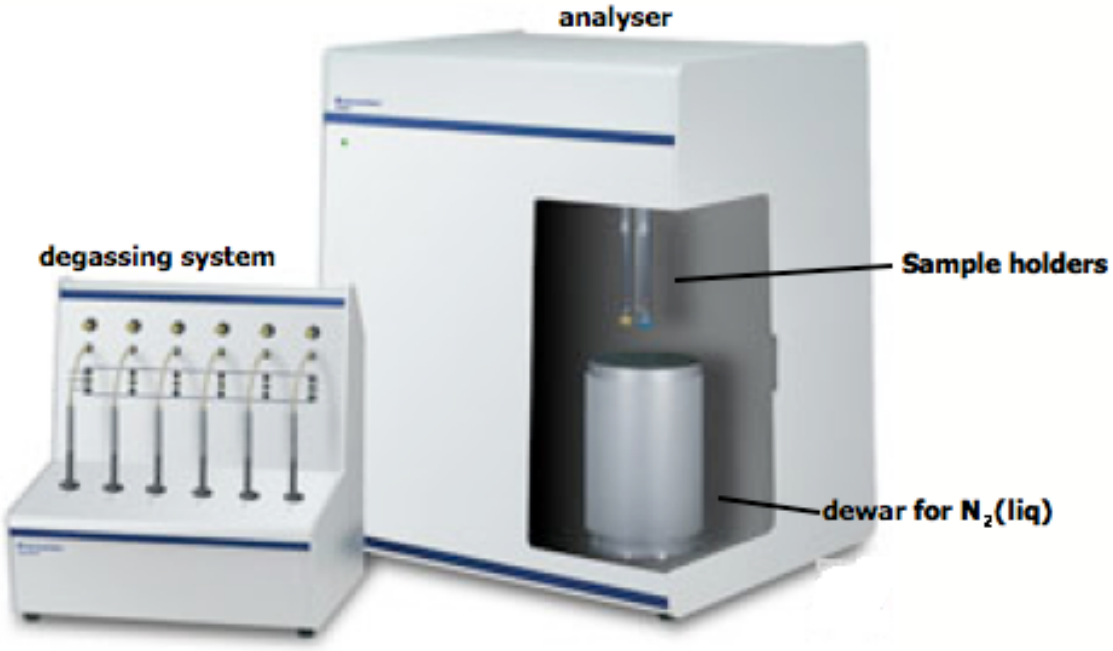

Figure A.3: *A picture of TRISTAR 3000.*

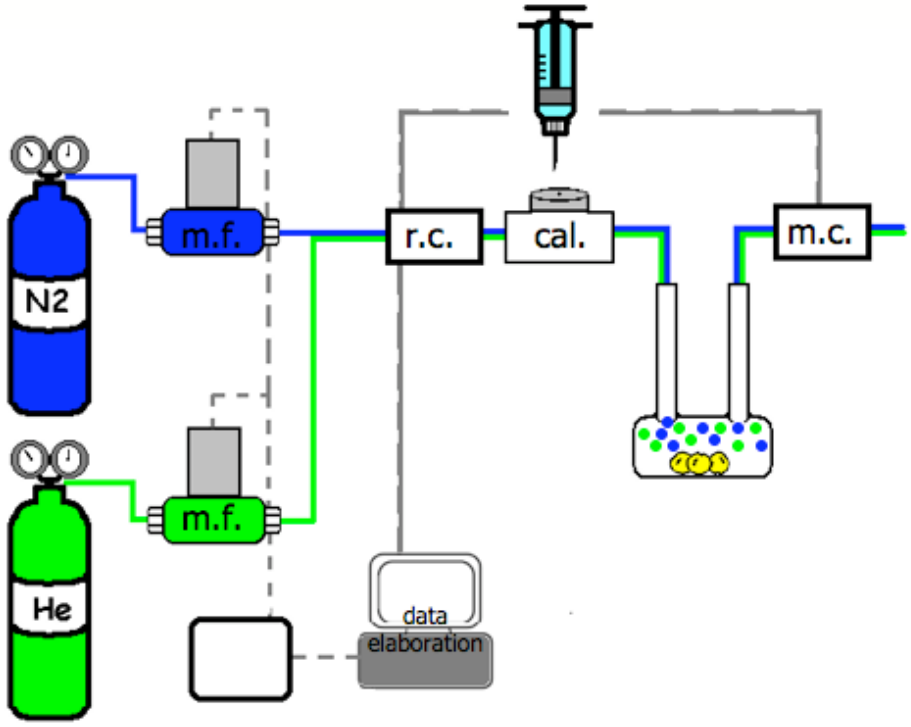

Figure A.4: *A depiction of the ChemBET 3000 apparatus. The He/N_2 mixture prepared by the two mass flowmeters (m.f.) passes through the reference cell (r.c.), the calibration cell (cal.), goes inside the sample holder and through the measurement cell (m.c.). All the TCD signals are elaborated by a computer and BET results are given.*

A.2.1 Measurement with ChemBET 3000

A scheme of the experimental apparatus with the gas line is depicted in Fig. A.4. Each measurement requires a mixture of He and N_2 (contained in the two gas bottles) at different concentrations prepared by two capillary mass flowmeters. When the gas mixture is inside the instrument, it passes before through the first branch (reference cell) of a thermal conductivity detector (TDC), then through a calibration cell and inside the sample holder and, in the end, in the measurement cell. The TCD monitors the processes of adsorption and desorption by measuring the change in the thermal conductivity of the gas mixture [65].

The sample must be weighed with an analytical balance and degassed to remove all the

impurities, which can be adsorbed on the surface of the pores of the sample. After heating at 450°C for about 3 h, the sample is ready for the measurement.

The mixture of He and N_2 fills the apparatus, passing through the reference and the measurement cells, which detect the two gas concentrations. The mixture is inside the sample holder (a quartz cell), thus the powder is exposed to such concentrations of He and N_2. The second step consists in dipping the sample holder into a dewar full of liquid N_2, which is physisorbed on the powder. As a consequence of N_2 adsorption, the atmosphere in the sample holder becomes reacher in He. Thereby, the TCD detects the gas concentration change, which corresponds to the adsorption signal. The bath of liquid N_2 is removed, so that the gas can desorb from the sample and enriches the mixture, generating the desorption signal, detected by the TCD. In the end, the two signals are calibrated by injecting a known quantity of N_2 with a syringe. The calibration signal is detected and used to calculate the desorbed quantity, V_{des}:

$$V_{des} = V_{cal}\frac{A_{des}}{A_{cal}} \tag{A.7}$$

V_{cal} is the quantity in the syringe, A_{des} and A_{cal} the areas of the desorption and calibration signals, respectively (see Fig. A.5 for a depiction of TCD signal). V_{des} must be changed into standard conditions of temperature and pressure (STP: 0°C or 273.15 K and 1 atm or 1013.25 mbar):

$$V_{des}(STP) = V_{des}\frac{273.15}{273.15+T}\cdot\frac{p}{1013.25} \tag{A.8}$$

Pressure, p, and temperature, T, are expressed in mbar and °C, respectively. The adsorbed quantity, W_{ads}, is given by the following expression:

$$W_{ads} = V_{des}(STP)\frac{p_s M}{RT_s} \tag{A.9}$$

p_s is the standard pressure in atm and T_s the standard temperature in K. Once obtained W_{ads}, which is equal to W_{mon}, one can calculate surface specific area through Eqs. A.3, A.5 and A.6.

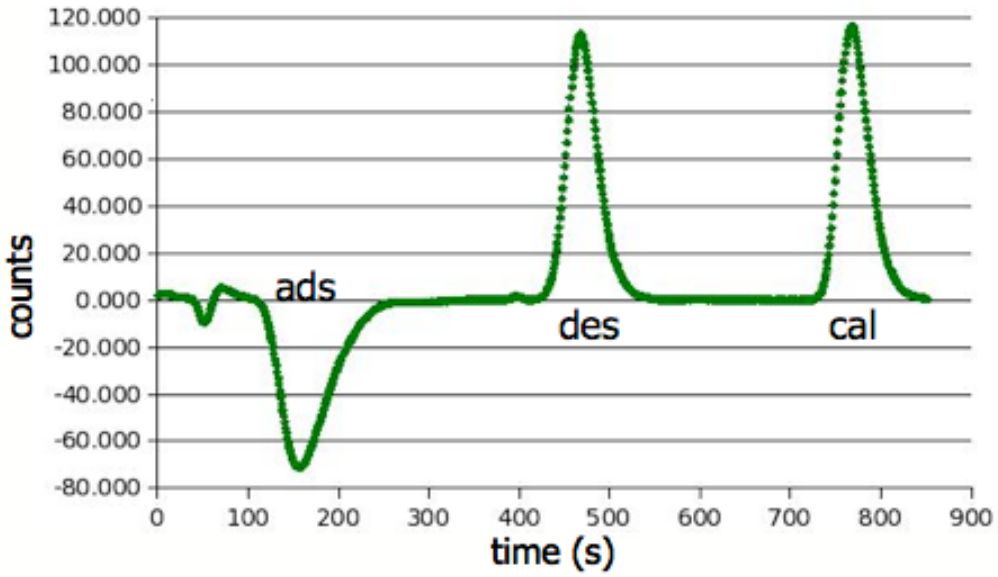

Figure A.5: *Signals generated by adsorption (ads) and desorption (des) processes and calibration signal (cal). During the desorption process, the gas leaving the sample cell is reacher in adsorbate. Therefore, the signal is opposite in polarity to that obtained during adsorption. The calibration signal must be very similar in shape and intensity to the sample signals [65].*

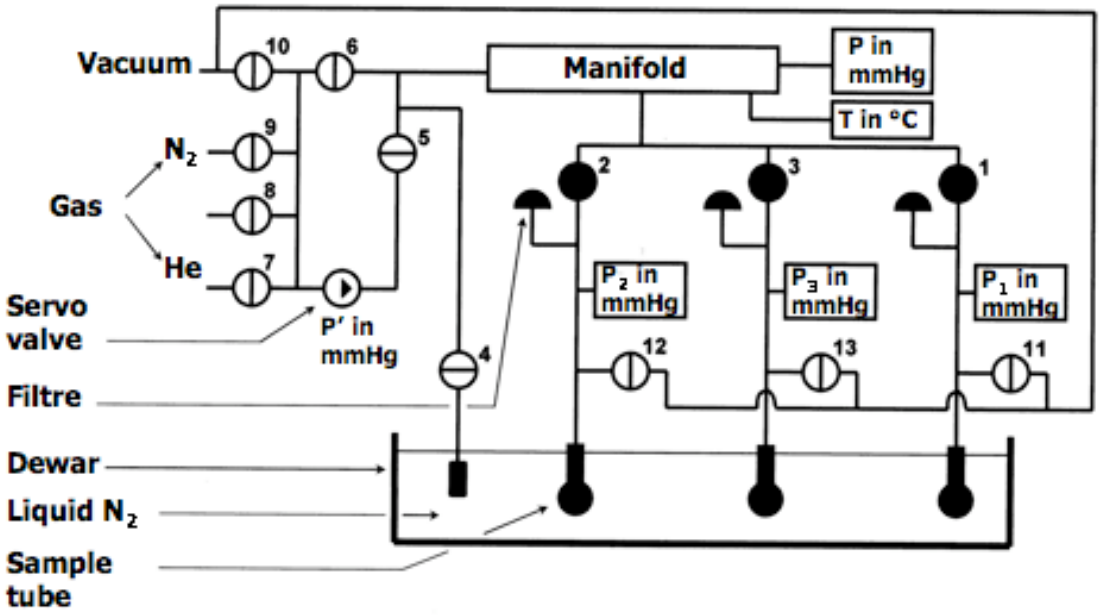

Figure A.6: *A scheme of the TRISTAR 3000. P is the pressure at the level of the gas collector; P_1, P_2 and P_3 are the pressures at the level of the analysis port 1, 2 and 3; P' is the pressure requested by the servo-valve in a direction or in the other; T is the temperature inside the instrument.*

A.2.2 Measurement with TRISTAR 3000

The whole apparatus is equipped with a degassing system, with an automatic analyser, with a vacuum pump and with a control module (see Fig. A.6 for a scheme of the apparatus). The degassing system can work under vacuum or under inert gas stream. It consists of six sample ports, each independently controlled. The analyser comprises three independent sample ports and four detectors of pression (one for each sample station and one for the gas manifold), allowing independent and simultaneous analysis of three samples [66].

The weighed sample is degassed under vacuum (0.1 mbar) at 300°C for 2 h and 30 min. After the degassing phase, the sample is weighed again before the beginning of the effective measurement. Then, the sample contained in an evacuated tube is cooled to the temperature of liquid N_2 and subsequently exposed to analysis gas (N_2) at a series of precisely controlled pressures. With each incremental pressure increase, the number of gas

molecules adsorbed on the surface increases. The equilibrium pressure, p, is compared to the saturation pressure, p_0, and their relative pressure ratio, p/p_0, is related to the quantity of gas adsorbed by the sample at each equilibrium pressure. As adsorption proceeds, the thickness of the adsorbed film increases. All the micropores are filled first, then the free surface becomes completely covered, and finally the larger pores are filled by capillary condensation. The process may continue to the point of bulk condensation of the analysis gas. Then, the desorption process can begin by systematically reducing pressure. As with the adsorption process, the quantity of gas desorbed from the solid surface at each decreasing equilibrium pressure is quantified. These two sets of data describe the adsorption and desorption isotherms. Signals are elaborated to give the specific surface area value (by multipoint method) [66, 67].

Bibliography

[1] C. Wagner, K. Hauffe, *Ztschr. Elektrochem.*, **33**, (1938) 172.

[2] W.H. Brattain, J. Bardeen, *Monograph*, (Bell Telephone System Tech. Publs., 1953).

[3] G. Heiland, *Z. Phys.*, **138**, (1954) 459.

[4] S.R. Morrison, *Adv. Catal.*, **7**, (1955) 259.

[5] T. Seiyama, A. Kato, K. Fujiishi, M. Nagatani, *Anal. Chem.*, **34**, (1962) 1502.

[6] N. Taguchi, *Gas detecting device, U.S. Patent No.3631436*, (1971).

[7] M.J. Madou, S.R. Morrison, *Chemical Sensing with Solid State Devices*, (Academic Press, Inc., 1989).

[8] S. Gherardi, *Master thesis*, (2001).

[9] P. Ciureanu, S. Middelhoek, *Thin Film Resistive Sensors*, (IOP Publishing, Bristol, UK, 1992).

[10] C. Malagù, V. Guidi, M. Stefancich, M.C. Carotta, G. Martinelli *J. App. Phys.*, **91**, (2002) 808-814.

[11] N. Barsan, U. Weimar, *J. Electroceram.*, **7**, (2001) 143-167.

[12] M. C. Carotta, G. Martinelli, L. Crema, C. Malagù, M. Merli, G. Ghiotti, *Sens. Actuators, B*, **76**, (2001) 336-342.

[13] N. Barsan, D. Koziej, U. Weimar, *Sens. Actuators, B*, **121**, (2007) 18.

[14] X. Du, Y. Du, S. M. George, *J. Phys. Chem. A*, **112**, (2008) 9211-9219.

[15] A. Gurlo, R. Riedel, *Angew. Chem. Int. Ed.*, **46**, (2007) 3826.

[16] J. N. Zemel, *Thin Solid Films*, **163**, (1988) 189.

[17] D.J. Shaw, S. Middelhoek, *Introduction to Colloid and Surface Chemistry*, (Butterworth-Heinemann, Oxford, UK, 1966).

[18] S.L.M. Schroeder, M. Gottfried, (2002) 1-22.

[19] P. Atkins, *Physical Chemistry*, (Oxford University Press, UK, 1998).

[20] S. Lowell, J. E. Shields, *Powder Surface Area and Porosity*, (Kluwer Academic Publishers, UK, 1991).

[21] P. Webb, *MIC Technical Publications*, (2003) 1-12.

[22] C.J. Brinker, G.W. Scherer, *Sol-Gel Science: The Physics and Chemistry of Sol-Gel Processing*, (Academic Press, New York, 1990).

[23] C. Malagù, *PhD thesis*, (2001).

[24] A. Giberti, *PhD thesis*, (2004).

[25] E. Traversa, M. L. Di Vona, S. Licoccia, M. Sacerdoti, M. C. Carotta, L. Crema, G. Martinelli, *J. Sol-Gel Sci. Technol.*, **22**, (2001) 167-179.

[26] M. C. Carotta, B. Cavicchi, M. Ferroni, V. Guidi, C. Malagù, G. Martinelli, C. Contado, F. Dondi, *proc. of Electroceramics VIII*, (August 25-28, 2002, Rome, Italy).

[27] M. C. Carotta, B. Cavicchi, M. Ferroni, V. Guidi, C. Malagù, G. Martinelli, M. L. Di Vona, S. Licoccia, E. Traversa, *proc. of Electroceramics VIII*, (August 25-28, 2002, Rome, Italy).

[28] J.P. Joly, *C.R. Acad. Sci. Paris*, **295**, 1982 717.

[29] F. Gaillard, M. Abdat, J.P. Joly, A. Perrard, *Appl. Surf. Sci.*, **238**, 2004 91.

[30] J.P. Joly, A. Perrard, *Langmuir*, **17**, (2001) 1538-1542.

[31] M.A. Alvarez-Merino, J.P. Joly, F. Carrasco-Marin, C. Moreno-Castilla, *Colloid Interface Sci.*, **260**, (2003) 449-453.

[32] D. Puzzovio, M.C. Carotta, A. Cervi, A. El Hachimi, J.P. Joly, F. Gaillard, V. Guidi, *submitted to Solid State Ionics*.

[33] A. Chiorino, G. Ghiotti, F. Prinetto, M.C. Carotta, D. Gnani, G. Martinelli, *Sens. Actuators, B*, **58**, (1999) 338-349.

[34] M.C. Carotta, S. Gherardi, C. Malag, M. Nagliati, B. Vendemiati, G. Martinelli, M. Sacerdoti, I.G. Lesci, *Thin Solid Films*, **515**, (2007) 8339-8344.

[35] M.C. Carotta, S. Gherardi, V. Guidi, C. Malag, G. Martinelli, B. Vendemiati, M. Sacerdoti, G. Ghiotti, S. Morandi, A. Bismuto, P. Maddalena, A. Setaro, *Sens. Actuators, B*, **130**, (2008) 38-45.

[36] F. Gaillard, J.-P. Joly, A. Perrard, *Ads. Sci. Technol.*, **25**, (2007) 245.

[37] M. Iwamoto, Y. Yoda, N. Yamazoe, T. Seiyama, *J. Phys. Chem*, **82**, (1978) 2564.

[38] A. Perrard, J.P. Joly, J.E. Germain, *C.R. Acad. Sci. Paris*, **297, Série II**, (1983) 799.

[39] R.I. Masel, *Principles of Adsorption and Reaction on Solid Surfaces*, (John Wiley&Sons, New York, 1996).

[40] A. Bielanski, J. Haber, *Catal. Rev. Sci. Eng.*, **19** (1979) 1.

[41] K. Wada, M. Egashira, *Sens. Actuators, B*, **B53**, (1998) 147.

[42] G. Sarala Devi, S. V. Manorama, V. J. Rao, *Sens. Actuators, B*, **B56**, (1999) 98.

[43] J. Oviedo, M.J. Gillan, *Surf. Sci*, **490**, (2001) 221.

[44] M. Che, A. J. Tench, *Adv. Catal.*, **31**, (1982) 77.

[45] R. Sanjines, F. Levy, V. Demarne, A. Grisel, *Sens. Actuators, B*, **B1**, (1990) 176.

[46] D. Kohl, L. Heinert, J. Bock, T. Hofmann, P. Schieberle, *Sens. Actuators, B*, **70**, (2000) 43-50.

[47] D. Koziej, N. Barsan, V. Hoffmann, J. Szuber, U. Weimar, *Sens. Actuators, B*, **108**, (2005) 75-83.

[48] D.P. Mann, T. Paraskeva, K.F.E. Pratt, I.P. Parkin, D.E. Williams, *Meas. Sci. Technol.*, textbf16, (2005) 1193-1200.

[49] S. Chakraborty, A. Sen, H.S. Maiti, *Sens. Actuators, B*, **115**, (2006) 610-615.

[50] H.H. Kung, *Adv. Catal.*, **40**, (1994) 1.

[51] I.C. Marcu, J.M. Millet, J.M. Herrmann, *Catal. Lett.*, **78**, (2002) 273-279.

[52] I.C.Marcu,J.M.Millet,I.Sandulescu, *J.Serb.Chem.Soc.*, **70**, (2005) 791-798.

[53] A. Chiorino, G. Ghiotti, F. Prinetto, M.C. Carotta, D. Gnani, G. Martinelli, *Sens. Actuators, B*, **58**, (1999) 338-349.

[54] N. Yamazoe, J. Fuchigami, M. Kishikawa, T. Seyama, *Surf. Sci.*, **86**, (1979) 335-344.

[55] J. Lausmaa, P. Löfgren, B. Kasemo, *J. Biomed. Mater. Res.*, **44**, (1999) 227-242.

[56] M.C. Carotta, A. Cervi, A. Giberti, V. Guidi, C. Malagù, G. Martinelli, D. Puzzovio, *Sens. Actuators, B*, **136**, (2009) 405-409.

[57] M.C. Carotta, A. Cervi, A. Giberti, V. Guidi, C. Malagù, G. Martinelli, D. Puzzovio, *Sens. Actuators, B*, **133**, (2008) 516-520.

[58] V.S. Vaishnav, P.D. Patel, N.G. Patel, *Thin Solid Films*, **490**, (2005)94-100.

[59] V. Guidi, M.C. Carotta, G. Martinelli, M. Nagliati, D. Puzzovio, D. Vecchi, *Sens. Actuators, B*, **133**, (2008) 516-520.

[60] V. Guidi, M.C. Carotta, G. Martinelli, M. Nagliati, D. Puzzovio, *submitted to Sens. Actuators, B.*

[61] A. Giberti, M.C. Carotta, V. Guidi, C. Malagù, G. Martinelli, M. Piga, B. Vendemmiati, *Sens. Actuators, B*, **103**, (2004) 272-276.

[62] M. Benetti, *Master thesis*, (2005).

[63] portal.jce.ac.il/courses/nano/Characterization%202006/02.%20bet.ppt.

[64] http://www.reolab.unimo.it/bet/sld013.htm.

[65] ChemBET 3000 operation manual.

[66] TRISTAR 3000 manuel d'utilisation.

[67] http://www.micromeritics.com.

List of publications

D. Puzzovio, M.C. Carotta, A. Cervi, A. El Hachimi, J.P. Joly, F. Gaillard, V. Guidi, *TPD and ITPD study of materials used as chemoresistive gas sensors*, submitted to Solid State Ionics.

M.C. Carotta, A. Cervi, A. Giberti, V. Guidi, C. Malagù, G. Martinelli, D. Puzzovio, *Ethanol interference in light alkane sensing by metal-oxide solid solutions*, Sens. Actuators, B, **136**, (2009) 405-409.

M.C. Carotta, A. Cervi, V. di Natale, S. Gherardi, A. Giberti, V. Guidi, D. Puzzovio, B. Vendemiati, G. Martinelli, M. Sacerdoti, D. Calestani, A. Zappettini, M. Zha, L. Zanotti, *ZnO gas sensors: A comparison between nanoparticles and nanotetrapods-based thick films*, in press on Sens. Actuators, B.

M.C. Carotta, A. Cervi, A. Giberti, V. Guidi, C. Malagù, G. Martinelli, D. Puzzovio, *Metal-oxide solid solutions for light alkane sensing*, Sens. Actuators, B, **133**, (2008) 516-520.

V. Guidi, M.C. Carotta, G. Martinelli, M. Nagliati, D. Puzzovio, *Sensing of alkanes and hydrogen by solid solutions of metal-oxide*, submitted to Sens. Actuators, B.

V. Guidi, M.C. Carotta, G. Martinelli, M. Nagliati, D. Puzzovio, D. Vecchi, *Sensing of volatile alkanes by metal-oxide semiconductors*, Sens. Actuators, B, **133**, (2008) 516-520.